Martina Kreuzbichler, BSc. (01231538)

Calibration of Acoustic Particle Velocity Sensors

Master's Thesis

to achieve the university degree of

Diplom-Ingenieurin

Master's degree programme: Electrical Engineering and Audio Engineering

submitted to

Graz University of Technology

Assessor

Priv.-Doz. Dipl.-Ing. Dr. Anton Fuchs

Supervisors

Eugène Nijman, M.Sc
Dipl.-Ing. Dr. Jan Rejlek

Institute of Electrical Measurement and Measurement Signal Processing

in cooperation with VIRTUAL VEHICLE

Graz, March 2018

Affidavit

I declare that I have authored this thesis independently, that I have not used other than the declared sources/resources, and that I have explicitly indicated all material which has been quoted either literally or by content from the sources used. The text document uploaded to TUGRAZonline is identical to the present master's thesis.

Date	Signature

Abstract

To be able to relate the output of an acoustic particle velocity sensor correctly to the physical quantity, a reliable calibration procedure for this sensor is crucial. The lack of a standardized procedure and the variations in the calibration curves obtained with different methodologies encourage the development of a new procedure. This thesis gives an overview of some calibration methods used so far and presents a calibration method using a vibrating piston. The pressure sound field above the piston is measured and analyzed in different layers above the piston. In a next step, various calculation methods (finite difference and holography) are tested to obtain particle velocity from pressure measurements. This velocity can be used as reference for a subsequent calibration. The calculated reference velocity is analyzed in terms of stability and precision, using simulated and measured pressure data. In order to perform the calibration in a fast and stable manner the work finally focuses on the finite difference method. With the help of measurements and finite difference, a stable vectorial velocity sound field above the piston is found. There, the acoustic particle velocity sensor can be calibrated and the influence of position errors is analyzed. In the end, a guide for calibration within a total precision is presented.

Kurzfassung

Um die gemessenen Werte eines Schallschnelle-Sensors korrekt mit den physikalischen Größen zu verknüpfen, ist es wichtig, ein zuverlässiges Kalibrationsverfahren zu haben. Da es derzeit noch keinen standardisierten Ablauf dafür gibt und die Ergebnisse mit verschiedenen Kalibrationsmethoden variieren, wird eine neue Kalibrationsmethode entwickelt. In dieser Arbeit werden zuerst verschiede derzeit benutze Prozeduren vorgestellt und ein Kalibrationsverfahren mit einem vibrierenden Kolben präsentiert. Die Schalldruckverteilung über diesem Kolben wird in verschiedenen Abständen gemessen und analysiert. Im nächsten Schritt werden unterschiedliche Methoden (Finite-Differenzen, Holografie) getestet, mit welchen es möglich ist, die Schallschnelle aus den Schalldruckwerten auszurechnen. Diese berechnete Schallschnelle kann dann als Referenzschnelle für die Kalibrierung verwendet werden. Die Stabilität und die Genauigkeit der Referenzschnelle werden mit simulierten als auch mit gemessenen Schalldruckdaten analysiert. Um die Kalibrierung schnell und stabil durchführen zu können, liegt das Hauptaugenmerk schlussendlich auf der Finiten-Differenzen-Methode. Durch Messungen und der Anwendung der Finiten-Differenzen-Methode kann ein stabiles vektorielles Schallschnellefeld über dem Kolben gefunden werden. Im Bereich dieses stabilen Feldes kann nun der Schallschnelle-Sensor kalibriert und Fehler auf Grund unzureichender Positionierungsgenauigkeit analysiert werden. Am Ende der Arbeit wird ein Leitfaden für eine Kalibrierung innerhalb einer gewissen Toleranz präsentiert.

Acknowledgments

This publication was written at VIRTUAL VEHICLE Research Center in Graz, Austria. I would like to acknowledge the financial support of the COMET K2 – Competence Centers for Excellent Technologies Programme of the Federal Ministry for Transport, Innovation and Technology (bmvit), the Federal Ministry for Digital, Business and Enterprise (bmdw), the Austrian Research Promotion Agency (FFG), the Province of Styria and the Styrian Business Promotion Agency (SFG). I would also like to express my thanks to the supporting industrial project partner BMW. Moreover, I would like to thank the FEMtech Praktika Studentinnen 2017 initiative under the program "Talente" funded by the bmvit.

I would like to thank my advisors Anton Fuchs, Eugène Nijman and Jan Rejlek for the supervision of my thesis, all the interesting discussions, sharing their knowledge and experience and giving me the opportunity to write my thesis at VIRTUAL VEHICLE.

I would also like to thank all my colleagues at the NVH & friction department for their time, whenever I had questions or needed support, and for the enjoyable working environment.

Thanks to Christina, Michael, Moritz and Michele for the proofreading of this thesis.

I would like to express my gratitude towards my family, who always supported me throughout my whole studies in every possible way. Especially Michele, who has been on my side, since the very beginning of my college education!

Last but not least I would like to thank all my fellow students, who have become true friends over the years, for the wonderful time, joint experiences, team spirit and the infinite hours of laughter.

Contents

1 Introduction

1.1 Motivation

The area of Noise, Vibration and Harshness (NVH) has become an essential part of the vehicle development process and sound isolation materials and their vibro-acoustic properties are getting increasingly important.

Therefore, the international research and development center VIRTUAL VEHICLE developed a trim test rig (Tbox) (see figure 1.1). It is used for experimental characterization of these vibro-acoustic properties using the patch transfer function (PTF) coupling scheme (e.g. [1], [2], [3] and [4]). An acoustic liner is excited by a structural shaker at the lower surface and a speaker on the upper surface while sound pressure and acoustic particle velocity are measured by a combination of force transducers and accelerometers on the bottom surface as well as sound pressure - particle velocity (PU) probes on the top side. The main focus of this thesis lies on the calibration of the acoustic particle velocity sensor of the PU probes.

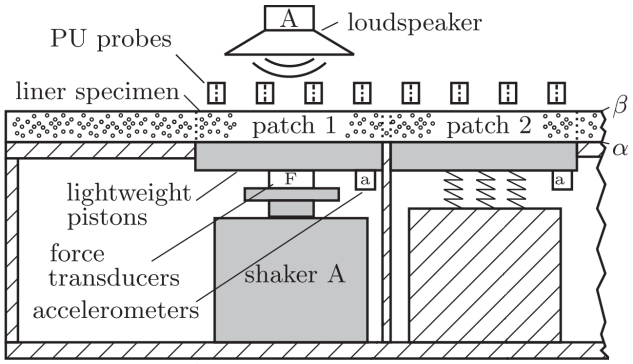

Figure 1.1: Trim test rig (Tbox) for experimental characterization of vibro-acoustic properties of sound isolation materials [1].

1.2 PU Probes

The Microflown sensor was invented in 1994. It indirectly measures the acoustic particle velocity of air, using two heated platinum wires with equal nominal resistance. The current generates heat in the wires, which is subsequently dissipated into the surrounding air. The main axis of the sensor is defined as the normal direction of the wires (see red arrow in the right side of figure 1.2. When particle velocity is propagating parallel to the direction of the sensor's main axis (across the wires), the wire which is reached first, cools down more than the other, resulting in a resistance difference, from which the acoustic particle velocity can be derived by means of a calibration curve. In a PU sensor, sound pressure and a particle velocity vector can be measured in almost the same spot (see figure 1.2). In general the PU sensor consists of two cylinders. One is hollow and contains the miniature sound pressure microphone. The other one is solid and contains the particle velocity sensor on top of it. The package protects the sensitive wires and amplifies the particle velocity gain.

An introduction to the technology and information about calibration, measurements and applications are given in [5]. This E-book was intended as a snapshot on ongoing research with the Microflown sensor, but unfortunately has not been updated since 2009.

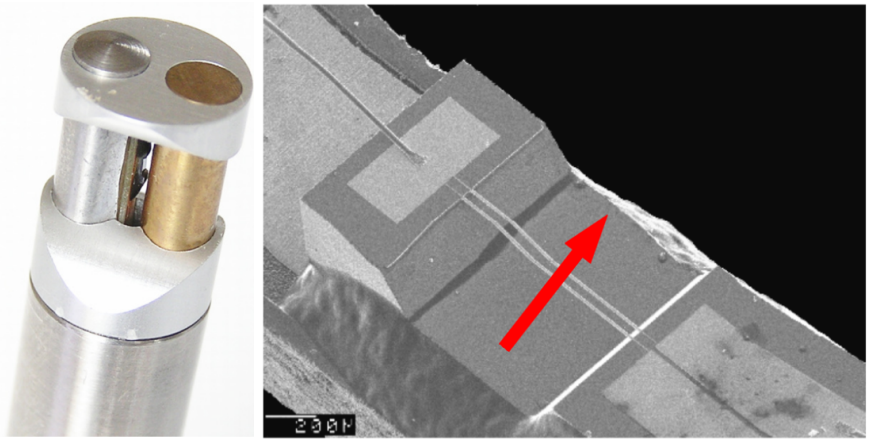

Figure 1.2: PU probe [5]; left figure: left cylinder: solid, particle velocity sensor mounted on side; right cylinder: hollow with enclosed microphone sensor; right figure: zoomed view of a bridge type Microflown particle velocity sensor, red arrow: main direction.

1.3 Calibration of Particle Velocity Sensors

The theory presented in this chapter is mainly based on the Microflown E-book [5].

To be able to relate the sensor output signal correctly to the physical quantity an accurate, stable and dependable calibration is needed. In comparison with sound pressure microphones or probes which measure the sound pressure at 2 different positions at a time (PP probes), no standardized calibration method for PU probes and acosutic particle velocity sensors exists. It is hence necessary to determine a correction factor between the amplitude/phase responses of the particle velocity and sound pressure sensor, since these are in general not equal. Until now, most of the used calibration methods involve a sound field with a known relationship between sound pressure and particle velocity and therefore a known acoustic impedance and environment [6].

The theoretical frequency response relates the particle velocity to the sound pressure and is therefore equal to the acoustic admittance H. The aim is to find a sound field where the impedance is known. Different methods are presented on the next pages. The equations for impedance and admittance can be found in various papers, e.g [5], [6], [7], [8] and [9].

1.3.1 Far Field Calibration in an Anechoic Chamber

For a propagating plane wave the acoustic admittance equals the reciprocal of the impedance

$$H = \frac{1}{\rho c}, \tag{1.1}$$

where ρ is the density of air and c is the speed of sound.

If the sound field is generated by a loudspeaker, it approximates a simple spherical field

$$H' = \frac{1}{\rho c}\left(1 + \frac{1}{ikr}\right), \tag{1.2}$$

where k is the wave number and r the distance between source an receiver position.

Far away from the source under free field conditions, kr is considerably larger than one and the second term in the brackets can be neglected. Although for

low frequencies, e.g. below 200 Hz the parenthesis factor is not negligible at, e.g. 5 m distance ($kr = \frac{2\pi f}{c} r = \frac{2\pi \cdot 200}{343} \cdot 5 = 18.3$) [6].

Therefore, a correction term $\frac{H'}{H}$ for the finite distance is introduced. For the amplitudes it is negligible, but for the phase term it is essential. However, the correction is less than perfect, because different measurement distances lead to slightly varying corrections. A reason for this is that an enclosed loudspeaker does not completely act as a monopole at a certain distance [6].

This leads to the conclusion that one shall measure as far away as possible from the source. But for low frequencies no anechoic room with the necessary size exists and with increasing distance the sound level reduces, thereby decreasing the signal to noise ratio. This fact makes it hard to acquire high quality measurements. If the anechoic chamber is too small for the use of an ordinary loudspeaker a more specific source is needed e.g. a "coincident source" loudspeaker mounted in a sphere.

The measured phase response of the particle velocity and sound pressure sensor in an anechoic chamber should be zero degrees, so the correction equals the inverse of the measured phase shift.

1.3.2 Near Field Calibration

As shown in the section above it is hard to achieve free field conditions. The next calibration procedure presented is conducted in the near field, where the sound levels are high. Thus reflections do not have a significant influence and the measurements can be carried out in an ordinary room. At a distance of 5 to 70 cm the probe position uncertainties are reduced and the small frequency dependent placement of the point source does not play an important role. On the downside, at a close probe position (e.g. 5 cm), the near field only exists for lower frequencies (transition at approx. $kr = 1$).

Monopole on a Plane Baffle

If the sound field is generated with a monopole, the acoustic admittance in equation 1.2 can be used in the near field. A small circular hole in a large plane baffle and a loudspeaker close to the baffle on the other side serve as a monopole and generate a spherical sound field in a half space [7].

One of the problems is the increasing particle velocity in the near field relative to the sound pressure (observable by applying equation 1.2). Therefore, the

distance between the hole and the transducer must be known exactly. Additionally, the scattering due to the transducer and the reflections of the baffle lead to further errors [7].

Piston on a Plane Baffle

If the wavelength is much bigger than the hole dimensions, the resulting source can be regarded as a piston on a plane baffle.

Monopole in a Sphere

The reflections from the finite baffle edges and the loudspeaker reaction are inevitable. If a spherical baffle is used, there are no edges and it can be made very stiff. Therefore a loudspeaker is put into a hollow sphere with a small hole. The specific acoustic admittances in front of the planar baffle and the sphere at a distance of 5 cm are similar [7].

Piston in a Sphere

The hole cannot be infinitely small to simulate a monopole exactly. Consequently, one might consider it as a small piston in a sphere [7]. The best calibration results are obtained in an anechoic room, but the results in an ordinary room do not deviate much.

Basten and de Bree [8] used a "real" piston in a sphere for calibration and extended the methodology for lower frequencies, because the results for low frequencies are unreliable due to dominant background noise in the measurements and low sound pressure level. The methodology is described on the next page.

For the calibration, a spherical loudspeaker with known acoustic impedance is used (see figure 1.3). It can be modeled as a sphere and a moving piston and therefore, the impedance is known.

For high frequencies, the probe is characterized via the reference microphone p_{ref}, which is positioned at a certain distance in front of the speaker next to the probe, and the known normalized impedance Z (see figure 1.3 a). For the absolute value and the angle pressure calibration in the frequency domain follows [10]:

$$|p_{\text{diff}}| = \frac{|p_{\text{probe}}|}{|p_{\text{ref}}|} \tag{1.3}$$

$$\angle(p_{\text{diff}}) = \angle(p_{\text{probe}}) - \angle(p_{\text{ref}}) \tag{1.4}$$

The calibration functions for the particle velocity can be written as [10]:

$$|v_{\text{ref}}| = \frac{|p_{\text{ref}}|}{|Z|} \tag{1.5}$$

$$\angle(v_{\text{ref}}) = \angle(p_{\text{ref}}) - \angle(Z) \tag{1.6}$$

$$|v_{\text{diff}}| = \frac{|v_{\text{probe}}|}{|v_{\text{ref}}|} \tag{1.7}$$

$$\angle(v_{\text{diff}}) = \angle(v_{\text{probe}}) - \angle(v_{\text{ref}}) \tag{1.8}$$

The sound pressure calibration can be used over the whole frequency range (20 - 10000 Hz), because the comparison between reference and probe microphone used for the calibration is based on omnidirectional signals at the same position. The background noise has no influence, because it does not matter if the calibration result relies on the speaker output or on noise. For the particle velocity this is not true, because the calculation relies on the known impedance Z due to the loudspeaker.

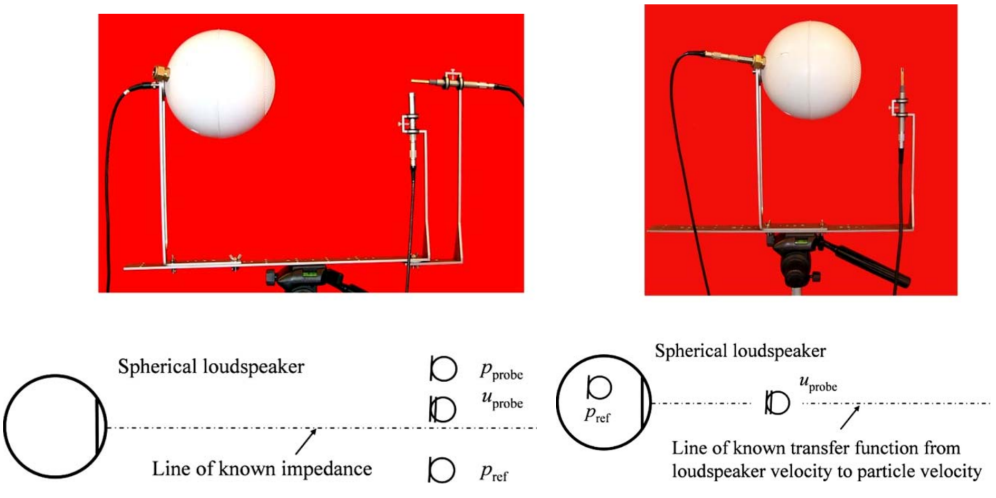

(a) Setup for high frequencies (b) Setup for low frequencies

Figure 1.3: Measurement setup for piston in a sphere calibration [8].

Consequently, another method for low frequencies must be used (see figure 1.3 b). The reference microphone is placed inside the sphere to achieve good SNR. If the interior sound pressure is known, the particle velocity at a distance r can be calculated. For more details the reader can refer to [8]. This known particle velocity is then used as reference velocity for calibration for frequencies well below the resonance frequencies of the sphere itself.

In the end the two calibration functions are connected at approximately 350 Hz with an amplitude tune for low frequencies and a phase tune for high frequencies.

1.3.3 Impedance Tube Calibration

Another method is the calibration in a standing wave tube, in which the impedance is known exactly. Unfortunately, it can only be used for frequencies below f_{g} which depends on the diameter of the tube and the speed of sound [8]

$$f_{\mathrm{g}} = \frac{c}{1.71d}. \tag{1.9}$$

1.3.4 Calibration with a Laser

In [11] an overview and experimental investigation on calibration with a laser based method is given. An advantage of this method is the absolute calibration of the particle velocity sensor without a pressure dependency. In the paper only the amplitude is calibrated over a frequency range of 500 Hz to 8000 Hz. The calibration process is expensive and time consuming, because it has to be repeated over discrete frequencies.

1.3.5 Calibration with Near Field Acoustical Holography

In [12] the acoustic impedance of the sound field is calculated with the measured sound pressure and particle velocity. If the impedance does not have a closed form solution it is reconstructed with the help of the equivalent source method, which is based on Near Field Acoustical Holography. At first, the sound pressure p_{probe} and the normal particle velocity v_{probe} are measured. The sensitivity S_p of p_{probe} can be determined with the help of a reference pressure sensor p_{ref}:

$$S_p = \frac{p_{\text{probe}}}{p_{\text{ref}}} S_{\text{ref}} \tag{1.10}$$

Secondly, the sound pressure p_{r} is reconstructed using v_{probe} and holography. Thirdly, the acoustic impedance $Z = \frac{p_{\text{r}}}{v_{\text{probe}}}$ is calculated. In the next step the calibration function (sensitivity) can be computed:

$$S_v = v_{\text{diff}} = \frac{v_{\text{probe}}}{p_{\text{ref}}} Z \; S_{\text{ref}} = \frac{v_{\text{probe}}}{p_{\text{ref}}} \frac{p_{\text{r}}}{v_{\text{probe}}} \frac{p_{\text{ref}}}{p_{\text{probe}}} S_p = \frac{p_{\text{r}}}{p_{\text{probe}}} S_p \tag{1.11}$$

The final sensitivity of the particle velocity sensor is computed via the average of all measurement points.

To be able to use holography, many positions, which cover an area bigger than the sound source, are needed and the frequency band is limited (for more details see chapter 2). Jing et al. [12] do two experiments with 196 (experiment 1) and 160 points (experiment 2) in a frequency range from 200 to 3000 Hz with 50 Hz spacing using a dodecahedron source (experiment 1) and a loudspeaker (experiment 2). The sensitivities obtained with these methods agree with the data given in the calibration report by the manufacturer.

1.3.6 Calibration with a Vibrating Piston

Metzger and Kaltenbacher use a circular piston for calibration of a 3D particle velocity sensor [13]. The circular plane produces a reference sound field and the output of the particle velocity sensor is compared to the acting particle velocity $\vec{v}_{\text{a}} \cdot \vec{n}_{\text{dir}}$ on the transducer. The particle velocity vector $\vec{v}_{\text{a}}$ is determined with FE simulation data of the reference sound field. The orientation $\vec{n}_{\text{dir}}$ is obtained with a 3D acceleration sensor and the local gravity field, which is pointing in the exact opposite direction (anti-parallel), compared to the surface velocity of the piston. Using laser vibrometer the velocity on the surface is determined and used as reference sound field. The particle velocity sensor is placed at a distance in front of the circular plane's center. The method presented by Metzger and Kaltenbacher requires a lot of equipment and even though they mention that the calibration is performed in an ordinary room without any anechoic conditions, the propagation region in the FE simulation is surrounded by a perfectly matched layer to model free radiation. Consequently, a part of the calibration needs free field conditions.

1.3.7 Summary of the Introduction

A variety of different acoustic particle velocity calibration methods exist up to now. In an anechoic room calibration results of good quality are obtained under free field conditions. However, an anechoic chamber is not available to everyone. Therefore, near field calibration methods are used as well. The most common one is known as piston in a sphere and can be used over the full bandwidth. A disadvantage of this method is, that the results measured in an anechoic room are still better than in an ordinary room where some corrections for reflections have to be applied. Furthermore the reference particle velocity depends on the measured acoustic pressure and the impedance estimated from a closed-form formula, so no absolute calibration can be carried out and there must be an extra calibration for low and high frequencies. This is time consuming and the connection of the two calibration functions is prone to errors. The calibration in the impedance tube can be performed for low frequencies only and the laser based method is time consuming and expensive. All methods presented lead to different calibration functions and some of them calibrate the amplitude only.

The aim of this work is to find a method, where the reference particle velocity field can be derived in a stable and absolute manner without the need of an anechoic chamber. In order to do so, the sound field is produced by a piston (as in [13]) and the sound pressure above the piston is measured in different layers. In a next step different calculation methods are tested (e.g. holography methods and finite difference) to obtain the acoustic particle velocity from sound pressure measurements, which then can be used as reference for the subsequent calibration. In all those measurements only sound pressure microphones are used and the particle velocity sensor is only needed in the final step, when the obtained reference velocity is used to calculate the sensitivity (calibration curve)

$$S_v = \frac{v_{\text{probe}}}{v_{\text{ref}}}. \tag{1.12}$$

2 Theory

The main goal of this thesis is to calculate the particle velocity with data from sound pressure measurements and use this velocity as a reference to calibrate the velocity sensor. This chapter presents the theory and shows how the reference velocity is obtained.

2.1 Planar Near Field Acoustical Holography

Near field Acoustical Holography (NAH) [14] is a tool to characterize radiating sources and to reconstruct sound fields. The sound pressure distribution is measured in a planar hologram, very close to the sources and thereby plane and evanescent waves are captured. With the help of Fourier transforms the pressure distribution can be expressed as a sum of propagating and evanescent waves. Once the angular spectrum is known it can be extrapolated to any other parallel plane in space. Afterwards, in this plane the pressure and / or the velocity can be obtained.

The following section deals with the derivations of the transformation based on [14], [15] and [16].

2.1.1 Waves

Plane waves in a homogeneous, source free sound field satisfy the acoustic wave equation

$$\nabla^2 p(\mathbf{r},t) - \frac{1}{c^2}\frac{\partial^2 p(\mathbf{r},t)}{\partial^2 t} = 0, \tag{2.1}$$

where $\nabla^2 = \frac{\partial^2}{\partial x^2} + \frac{\partial^2}{\partial y^2} + \frac{\partial^2}{\partial z^2}$, speed of sound $c = 343\,\frac{\mathrm{m}}{\mathrm{s}}$, position vector $\mathbf{r} \equiv (x,y,z)$.

If the method of separation of variables is used and an exponential solution guessed

$$p(\mathbf{r}, t) = p(\mathbf{r})e^{i\omega t}, \tag{2.2}$$

one ends up with one term depending on the position $\mathbf{r}$ and one term depending on the time t.

Insertion of equation 2.2 in 2.1 yields the Helmholtz equation

$$\nabla^2 p(\mathbf{r}, \omega) + k^2 p(\mathbf{r}, \omega) = 0, \tag{2.3}$$

where the acoustic wave number is $k = \frac{\omega}{c} = \frac{2\pi f}{c} = \frac{2\pi}{\lambda}$.

A solution to the Helmholtz equation is

$$p(\mathbf{r}, \omega) = P(k_x, k_y, \omega)e^{i(k_x x + k_y y + k_z z)}, \tag{2.4}$$

where $P(k_x, k_y, \omega)$ is the angular spectrum and $k^2 = k_x^2 + k_y^2 + k_z^2$. Choosing k_x and k_y as the independent variables and k_z as the depending variable leads to:

$$k_z^2 = k^2 - k_x^2 - k_y^2 \tag{2.5}$$

When k_x or $k_y > k$ the plane waves turn to evanescent waves

$$k_z = \pm i\sqrt{-k^2 + k_x^2 + k_y^2}, \tag{2.6}$$

which decay in amplitude in z-direction.

Evanescent waves only occur close to the source and therefore care must be taken to capture them with the measurements. Many evanescent waves with high amplitudes and measurement noise lead to numerical problems, regularization (see section 2.1.4) remedies this.

Figure 2.1 shows plane and evanescent waves and the corresponding representation in k-space.

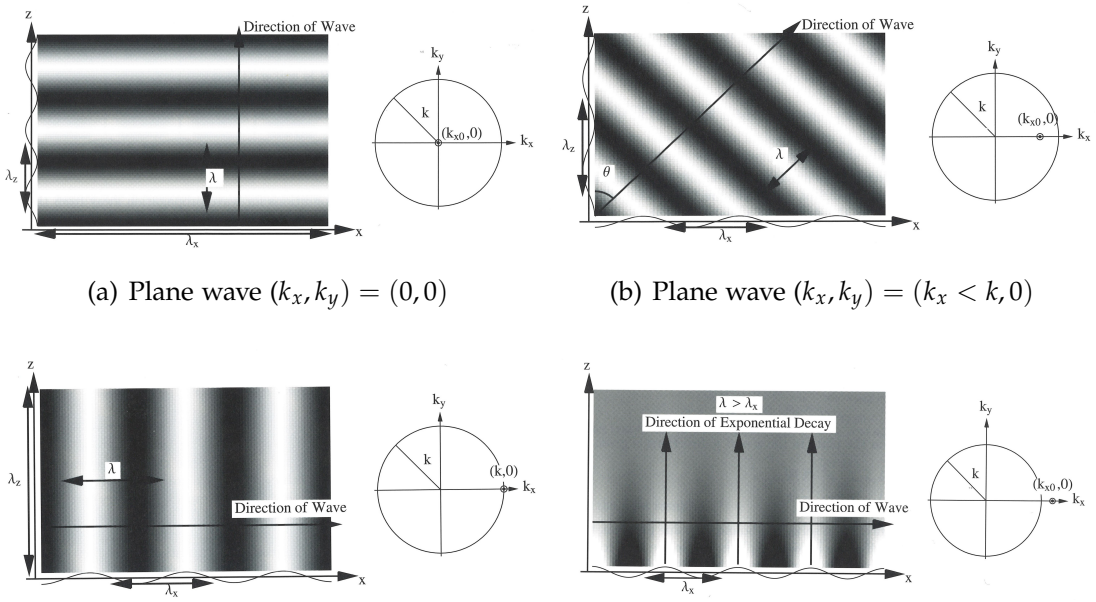

(a) Plane wave $(k_x, k_y) = (0, 0)$

(b) Plane wave $(k_x, k_y) = (k_x < k, 0)$

(c) Plane wave $(k_x, k_y) = (k, 0)$

(d) Evancescent wave $(k_x, k_y) = (k_x > k, 0)$

Figure 2.1: Waves and corresponding k-space representation. The circle defines the radiation circle with radius k [14].

2.1.2 Angular Spectrum

The plane and evanescent waves which form the sound pressure at a point may have different amplitudes and phases. These are taken into account with the angular spectrum $P(k_x, k_y)$.

The general form of the pressure field can be expressed with an inverse 2D Fourier transform as follows:

$$p(\mathbf{r}) = \frac{1}{4\pi^2} \int_{-\infty}^{\infty} dk_x \int_{-\infty}^{\infty} dk_y \; P(k_x, k_y) e^{i(k_x x + k_y y + k_z z)} \tag{2.7}$$

For simplicity ω is dropped from the equation and assume that from now on all equations are in frequency domain.

In a plane $z = 0$ the angular spectrum is defined by a 2D Fourier transform:

$$P(k_x, k_y) = \int_{-\infty}^{\infty} dx \int_{-\infty}^{\infty} dy \; p(x, y, 0) e^{-i(k_x x + k_y y)} \tag{2.8}$$

2.1.3 Wave Field Extrapolation

If the angular spectrum in a plane $z = 0$ is known, the sound field can be extrapolated in any other plane in space:

$$P(k_x, k_y, z) = P(k_x, k_y)e^{ik_z z} \tag{2.9}$$

Or in a more general form propagating from a plane $z = z'$ to a plane $z = z$:

$$P(k_x, k_y, z) = P(k_x, k_y, z')e^{ik_z(z-z')} \tag{2.10}$$

In the plane wave case, the amplitudes only undergo a phase change.

Furthermore with the help of Euler's equation it is possible to relate the normal velocity in z-direction to pressure:

$$i\omega\rho v_z(\mathbf{r}) = \frac{\partial}{\partial z}p(\mathbf{r}) \tag{2.11}$$

2D Fourier transform:

$$\begin{aligned} i\omega\rho V_z(k_x, ky, z) &= ik_z P(k_x, k_y, z) \\ V_z(k_x, ky, z) &= \frac{k_z}{\rho ck}P(k_x, k_y, z')e^{ik_z(z-z')} \end{aligned} \tag{2.12}$$

2.1.4 Inverse Problem

The exponential decay of evanescent waves in positive z-direction leads to exponential-like amplifications when $z < z'$. As a consequence, NAH is prone to instability issues, because inaccuracies and noise in the measurement data "blow up". This behavior leads to an ill-posed inverse problem and the calculations will lead to disaster. Regularization methods are a way to deal with such a problem [17], [18]. Tikhonov regularization is chosen in this thesis. The forward problem in matrix form can be written as [17]:

$$\begin{aligned} p &= \mathbf{F}^{-1}\frac{\rho ck}{k_z}e^{ik_z(z-z')}\mathbf{F}v_z \\ &= \mathbf{F}^{-1}\mathbf{G}\mathbf{F}v_z \\ &= \mathbf{H}v_z \end{aligned} \tag{2.13}$$

The diagonal matrix **G** contains the direct k-space propagators. It is pre-multiplied by an inverse DFT matrix $\mathbf{F}^{-1}$ and post-multiplied by and DFT matrix **F**.

Leading to the inverse problem:

$$v_z = \mathbf{H}^{-1} p \tag{2.14}$$

Tikhonov Regularization

The direct inversion of H would not lead to an appropriate result. Thus, the regularized inverse $\mathbf{R}_\alpha$ is calculated

$$v_z = \mathbf{R}_\alpha p, \tag{2.15}$$

with

$$\mathbf{R}_\alpha = (\mathbf{H}^H \mathbf{H} + \alpha I)^{-1} \mathbf{H}^H. \tag{2.16}$$

$\alpha = 0$ leads to the pseudo inverse of **H**.

With the help of singular value decomposition (SVD) of the matrix **H** the regularization principle may be understood:

$$\mathbf{H} = \mathbf{U}\mathbf{S}\mathbf{V}^{\mathbf{H}} \tag{2.17}$$

where **U** and **V** are left and right unitary matrices and **S** is a diagonal matrix with singular values s_i.

This leads to

$$\mathbf{R}_\alpha = \mathbf{V}\mathrm{diag}\left(\frac{s_i^*}{|s_i^2| + \alpha}\right)\mathbf{U}^H, \tag{2.18}$$

with the smallest α value used as a function input being smaller than the smallest squared eigenvalue.

With Tikhonov regularization the impact of the eigenvalues for increasing α values (beginning with the smallest ones) is reduced. The shape of a k-space filter, which eliminates evanescent waves with large wave numbers, is determined and therefore, the ”blow up” of the noise in the inversion process is reduced.

Generalized Cross Validation

Several different methods exist to seek the best α-value for regularization [19]. The used method is generalized cross validation (GCV), because with this method, the knowledge of the noise variance is not required [17]. It determines the α-value by minimizing the function

$$J(\alpha) = \frac{||(I - \mathbf{H}\mathbf{R}_\alpha)p||^2}{[\mathrm{Tr}(I - \mathbf{H}\mathbf{R}_\alpha)]^2}. \tag{2.19}$$

GCV is also called the "leaving-one-out" method, because it basically removes a measurement point at the time. It uses this point as a reference for the reconstruction at the missing data point with the remaining points. The mean square difference is minimized with the optimal parameter.

The straightforward calculation would take a lot of time, because the inversion of $\mathbf{H}$ for every frequency step and the complete range of α leads to a high computational effort. In a paper by Williams [17] a much more time-efficient implementation of this algorithm is described, relying on a fundamental paper published in 1979 [20].

The GCV does not lead to an appropriate result, if the noise components in the measurement data are highly correlated [19].

Improved Tikhonov Regularization

Sometimes the standard Tikhonov regularization does not lead to a suitable result. Williams proposed an improved Tikhonov regularization [17]

$$\mathbf{R}_\alpha = (\mathbf{H}^H\mathbf{H} + \alpha\mathbf{L}^H\mathbf{L})^{-1}\mathbf{H}^H, \tag{2.20}$$

where $\mathbf{L} = F_1^\alpha\mathbf{V}^H$ and F_1^α: high pass k-space filter. For more details and exact filter implementation see [17].

2.1.5 Errors

Errors, which have to be taken into account are presented and explained in the following section.

Discrete Measurements and Finite Area

In section 2.1.4 the matrix of the discrete Fourier transform is already used. Physical measurements cannot measure every pressure value on a plane. Thus, discrete points over a finite area are measured. The spacing a is constant in x- and y-direction and at least two spatial samples per wave period are needed for a correct allocation in the wave number domain. Consequently, the spatial domain must be sampled twice as often as the highest present waveform frequency $k_{\max}$:

$$a \leq \frac{\lambda}{2} = \frac{\pi}{k_{\max}} \tag{2.21}$$

$$k_{\max} \leq k_{\text{Nyquist}} = \frac{1}{2} k_{\text{sample}} = \frac{\pi}{a} \tag{2.22}$$

This leads to a maximum frequency of:

$$f_{\max} = \frac{c}{2a} \tag{2.23}$$

With use of a finite measurement area, the sound pressure is assumed to be equal to zero outside the area leading to a multiplication with a rectangular window function. Components will be periodically repeated and appear as aliasing. Furthermore, evanescent waves will leak into the plane wave area and vice versa. The fact that the pressure drops to zero outside the aperture, when using an rectangular window, leads to a discontinuity at the edges and thus to a high concentration of high wave numbers and the ”blow up” in the inverse problem.

This effect can be reduced by using a smooth window e.g. a Tukey window [14], [21]. When this window is applied directly to the measurement data, one must take care that no data containing useful information is lost - e.g. sources of interest near the border. Therefore, the method of border padding is used. Samples are added at the edge of the array with the values of the border signals. Afterwards a Tukey window is applied to the new data set containing the border-padded as well as the measured part. The constant part of the window

is placed over the measured region and the cosine-tapered part smooths the new border-padded area [22].

It is required that the magnitude of the pressure field at the edges of the array is at least 30 dB lower, compared to the maximum array pressure and as a result, the array must be about twice as big as the source area[15]. A method which is trying to circumvent the need for a big array and hence attempts to reduce these errors is the so called Statistically Optimized Near Field Acoustical Holography (SONAH see section 2.2).

It has to be mentioned that the convolution procedure of the inverse problem is localized in space. This means that if the actual sources of interest are far enough away from the edge, the computed values should not be erroneous. Only the rim region should be influenced by the generated errors [14].

Measurement Distance

For a correct velocity calculation, evanescent waves are required. Due to their decaying characteristics and limited signal to noise ratio, these waves must be captured close to the source (see section 2.1.1). Valdivia and Williams [23] recommend a distance between a and $2a$ with a being the microphone spacing. According to Maynard et al. [24] the minimum resolvable distance is approximately

$$R \equiv \frac{\pi}{k_{\max}}. \tag{2.24}$$

With equation 2.21 follows:

$$R \geq a \tag{2.25}$$

For NAH it is necessary to measure evanescent wave components. Therefore the measurement distance must be close enough, that the amplitude of the components is still higher than the noise. As a result, the maximum observable wave number depends on the SNR and the measurement distance d. Assuming that both the maximum plane and evanescent wave have the same amplitude, the minimum resolvable distance R is presented in the following equation [22], with the denominator being the new upper limit for k_{max}

$$R = \frac{\pi}{\sqrt{k^2 + \left(\frac{\mathrm{SNR}\cdot\ln(10)}{20\cdot d}\right)^2}}. \tag{2.26}$$

Coupling of the Nyquist criterion and the resolution leads to the following inequality:

$$\sqrt{k^2 + \left(\frac{\mathrm{SNR} \cdot \ln(10)}{20 \cdot d}\right)^2} > k_{\mathrm{Nyquist}} \tag{2.27}$$

If the inequality holds, aliasing occurs. According to this theory a low dynamic range microphone array can be placed closer to the radiating object than one with a high dynamic range, because the high dynamic range microphone retrieves more information about the evanescent waves.

Finally, this knowledge satisfies the sampling theorem. Therefore, one cannot sample very close to the source where there may be high spatial frequency components due to evanescant waves [25].

In [15] Williams also gives a formula refering to his book [14] which connects the required spacing a and the measurement distance d:

$$a = \frac{27.2}{\mathrm{SNR}} d \tag{2.28}$$

Pressure measurements compared to velocity measurements

Jacobsen and Liu [25] compared the performance of particle velocity-based and pressure-based NAH. Among other things, they have discovered that it is better to use a velocity sensor than a pressure microphone for velocity calculation. Especially at the edges of the array the results are better. One reason could be that inaccuracies are caused by the propagation factor (see equations 2.13 and 2.14) for pressure to velocity holography, because high spatial frequencies are amplified.

2.2 Statistically Optimized Near Field Acoustical Holography

Due to the main limitation of classical NAH – requirement for full coverage with significant sound pressure level – Statistically Optimized Near Field Acoustical Holography has been developed (see e.g. [26] and [27]). The basic theory given in this section is also based on these papers.

The major advantage compared to NAH is the possibility of using a smaller measurement array (even smaller than the source - patch method) and an arbitrary measurement grid.

2.2.1 Basic Theory

In a source free homogeneous half space the complex time-harmonic sound pressure can be written by an infinite sum of wave functions representing plane propagating and evanescent waves:

$$\Phi_k(\mathbf{r}) = Fe^{i(K_x x + k_y y + k_z(z - z^+))} \tag{2.29}$$

where F is an amplitude weighting function an z^+ represents the virtual source plane where the wave functions are scaled.

The sound pressure at an arbitrary point $\mathbf{r} = (x, y, z > 0)$ can be expressed as a linear combination of measured pressure data $\mathbf{p}$

$$p(\mathbf{r}) = \mathbf{p}^T \mathbf{c}(\mathbf{r}), \tag{2.30}$$

where the transfer vector $\mathbf{c}(\mathbf{r})$ contains the position dependent complex estimation coefficients. This vector is obtained by the requirement that an infinite set of waves as written in equation 2.29 are projected in z-direction with high accuracy. In other words $p(\mathbf{r})$ in equation 2.30 is replaced by the value of a wave function at position $\mathbf{r}$ and $\mathbf{p}$ which contains the wave function values at the measurement positions, equation 2.30 must still hold. As a result, one obtains:

$$\boldsymbol{\alpha}(\mathbf{r}) \simeq \mathbf{A}\mathbf{c}(\mathbf{r}) \tag{2.31}$$

with vector $\boldsymbol{\alpha}(\mathbf{r})$ representing the values of the wave functions at the reconstruction point and matrix $\mathbf{A}$ containing the values of the wave functions at the measurement positions.

This leads to the least-squares solution:

$$\mathbf{c}(\mathbf{r}) = (\mathbf{A}^H \mathbf{A})^{-1} \mathbf{A}^H \boldsymbol{\alpha}(\mathbf{r}) \tag{2.32}$$

After the insert of equation 2.32 in equation 2.30 the following expression for the sound pressure at position $\mathbf{r}$ is obtained:

$$p(\mathbf{r}) = \mathbf{p}^T(\mathbf{A}^H\mathbf{A})^{-1}\mathbf{A}^H\boldsymbol{\alpha}(\mathbf{r}) \tag{2.33}$$

The equation for the velocity can be derived with the help of Euler's equation (see equation 2.11)

$$\rho c v_z(\mathbf{r}) = \mathbf{p}^T(\mathbf{A}^H\mathbf{A})^{-1}\mathbf{A}^H\boldsymbol{\beta}_z(\mathbf{r}), \tag{2.34}$$

where $\boldsymbol{\beta}(\mathbf{r})$ represents the scaled particle velocities of the wave functions $\boldsymbol{\beta}_z(\mathbf{r}) = \frac{k_z}{k}\Phi(\mathbf{r})$.

2.2.2 Inverse Problem and Regularization

In the next step the vector $\mathbf{q} \rightarrow \mathbf{q}^T \equiv \mathbf{p}^T(\mathbf{A}^H\mathbf{A})^{-1}$ is estimated. With the definition of matrix $\mathbf{C} = (\mathbf{A}^H\mathbf{A})^T$ one gets

$$\mathbf{Cq} = \mathbf{p}, \tag{2.35}$$

and the inverse problem

$$\mathbf{q} = \mathbf{C^{-1}p}. \tag{2.36}$$

Hald [27] uses an eigenvalue/eigenvector expansion of the matrix C to regularize the solution:

$$\mathbf{C} = \mathbf{VSV^H} \tag{2.37}$$

where the columns of $\mathbf{V}$ contain the eigenvectors and $\mathbf{S}$ is a diagonal matrix with non negative eigenvalues s_i. With the help of Tikhonov regularization and General Cross Validation the regularized solution of $\mathbf{q}$ can be calculated [17]:

$$\mathbf{q}_\alpha = \mathbf{V}\mathrm{diag}\left(\frac{s_i^*}{|s_i^2| + \alpha}\right)\mathbf{V}^H\mathbf{p} \tag{2.38}$$

This leads to the following equations for sound pressure

$$p(\mathbf{r}) = \mathbf{q}_\alpha^T(\mathbf{A}^H\boldsymbol{\alpha}(\mathbf{r})), \tag{2.39}$$

and particle velocity

$$\rho c v_z(\mathbf{r}) = \mathbf{q}_\alpha^T(\mathbf{A}^H \boldsymbol{\beta}_z(\mathbf{r})). \tag{2.40}$$

The advantage of this definition is that the calculation of the pressure and particle velocity can be done for multiple points $\mathbf{r}$ without new regularization.

2.2.3 Virtual Source Plane and Scaling Functions

In equation 2.29 two elements need to be further defined:

- virtual source plane
- scaling function

According to [26], the virtual source plane $z = z^+$ could be on the same z-axis position as the real source plane $z^+ = z_0^+$, but usually it should be placed behind that plane $z^+ < z_0^+$ as illustrated in figure 2.2. Optimal accuracy is achieved when $-1.5a \leq z^+ \leq -a$ with a representing the measurement grid spacing.

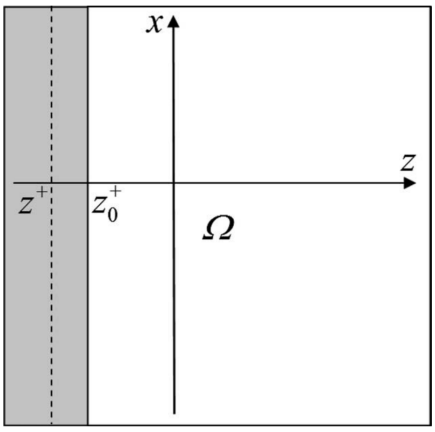

Figure 2.2: Measurement geometry in free field: source plane = vertical line, virtual source plane = dashed vertical line, Ω = domain for sound field representation [26].

When a unit weighting function

$$\mathbf{F}(k_z) = 1 \tag{2.41}$$

is used, all amplitudes of the plane wave functions have a value of one on the virtual source plane. Another scaling method is the omnidirectional weighting.

In this case all directions of plane-wave propagation are equally weighted inside the radiation circle

$$\mathbf{F}(k_z) = \sqrt{\frac{k}{k_z}}. \tag{2.42}$$

When the particle velocity is calculated (see equations 2.34 and 2.40) the evanescent wave components as well as errors and noise are amplified by the factor $\frac{|k_z|}{k}$ and could lead to a failing reconstruction. Therefore, a velocity scaling $\mathbf{F}(k_z) = \frac{k}{k_z}$ is defined. To avoid singularities, the velocity scaling function is modified to

$$\mathbf{F}(k_z) = \begin{cases} 1 & \text{for } \sqrt{k_x^2 + k_y^2} \leq k \\ \frac{k}{\sqrt{k^2 + |k_z|^2}} & \text{for } \sqrt{k_x^2 + k_y^2} > k. \end{cases} \tag{2.43}$$

In case of the velocity weighting the virtual source plane can be coincident with the real source plan and still lead to a stable reconstruction.

2.2.4 Errors

The errors are caused by the discrete spacing, the placement of the virtual source plane and the use of different scaling functions.

When using a discrete subset in the two-dimensional wave number domain one obtains

$$\Psi(\mathbf{r}) = \kappa \Phi_{k_n}(\mathbf{r}), \tag{2.44}$$

with $\kappa = \sqrt{\frac{\Delta k_x \Delta k_y}{2\pi k^2}}$ introducing a smooth transition when using discrete spectra.

With a discrete sample spacing the field in the wave number domain is spatially periodic and could lead to wrap-around errors (see section 2.1.5) [26].

If the sample spacing goes to zero, the matrix and vector multiplications $\mathbf{A}^H\mathbf{A}, \mathbf{A}^H\boldsymbol{\alpha}_z(\mathbf{r})\text{and}\mathbf{A}^H\boldsymbol{\beta}_z(\mathbf{r})$ can be calculated with infinite integrals.

Due to the different placements of the virtual source plane and the use of scaling functions, the accuracy of the reconstruction changes. As a consequence, it is difficult to verify the precision of the obtained results.

2.3 Finite Difference Method

With the finite difference (FD) method it is possible to approximate the pressure gradient from Euler's equation (see equation 2.11) and obtain the velocity

$$v_z(\mathbf{r}) = \frac{1}{i\omega\rho}\frac{\partial}{\partial z}p(\mathbf{r}) = \frac{1}{i\omega\rho}p'(z) \approx \frac{1}{i\omega\rho}\frac{p(z+\Delta z)-p(z)}{\Delta z}, \tag{2.45}$$

where $p(z+\Delta z)\text{and}p(z)$ are the measured sound pressures and Δz is the spacing in between.

2.3.1 Errors

Determination of the velocity error with Taylor series expansion

The approximation of the gradient with the FD scheme leads to an error for the velocity which can be determined with a Taylor series expansion:

$$p(z+\Delta z) = p(z) + p'(z)\frac{\Delta}{1!} + p''(z)\frac{\Delta^2}{2!} + p'''(z)\frac{\Delta^3}{3!} + ... \tag{2.46}$$

Rewriting the pressure $p(z) = pe^{-ikz}$ and reforming the equation leads to:

$$\begin{aligned}
\frac{p(z+\Delta z)-p(z)}{\Delta z} &= p'(z) - ikp'(z)\frac{\Delta}{2!} - k^2p'(z)\frac{\Delta^2}{3!} + ... \\
&= p'(z)\left(\frac{1}{k\Delta z}\left[k\Delta z - \frac{(k\Delta z)^3}{3!} + \frac{(k\Delta z)^5}{5!} - \frac{(k\Delta z)^7}{7!}...\right] + \right. \\
&\quad \left. \frac{i}{k\Delta z}\left[1 - \frac{(k\Delta z)^2}{2!} + \frac{(k\Delta z)^4}{4!} - \frac{(k\Delta z)^6}{6!}... - 1\right]\right) \\
&= p'(z)\left(\frac{\sin(k\Delta z)}{k\Delta z} + i\frac{\cos(k\Delta z)-1}{k\Delta z}\right)
\end{aligned} \tag{2.47}$$

For the absolute value follows:

$$\begin{aligned}\left|\frac{p(z+\Delta z)-p(z)}{\Delta z}\right| &= |p'(z)|\sqrt{\frac{2(1-\cos(k\Delta z))}{(k\Delta z)^2}} \\ &= |p'(z)|2\sqrt{\frac{\frac{1}{2}(1-\cos(k\Delta z))}{(k\Delta z)^2}} \\ &= |p'(z)|\frac{\sin\left(\frac{k\Delta z}{2}\right)}{\left(\frac{k\Delta z}{2}\right)}\end{aligned} \tag{2.48}$$

The same result for the finite difference velocity error is obtained by Schulz in [28].

Assuming a maximum error of 1 dB and rewriting $p'(z)\hat{=}v(z)$:

$$-1 = L_{v,error} = 10log\frac{|v(z)|\frac{\sin\left(\frac{k\Delta z}{2}\right)}{\left(\frac{k\Delta z}{2}\right)}}{|v(z)|} \tag{2.49}$$

A graphical solution (see figure 2.3) leads to a value of $k\Delta z = 2.3$.

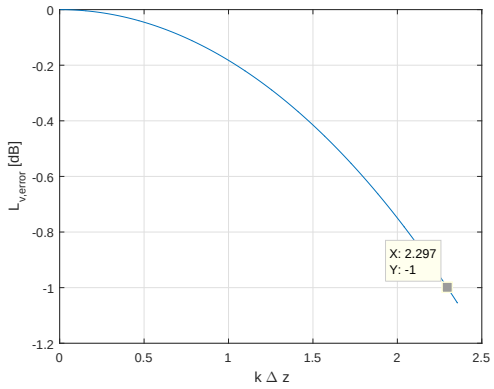

Figure 2.3: High frequency bias velocity error.

The upper frequency limit is then obtained as follows:

$$k\Delta z \leq 2.3 \rightarrow \frac{2\pi f\Delta z}{c} \leq 2.3 \rightarrow f_{v,\max} = \frac{2.3c}{2\pi\Delta z} \approx \frac{c}{3\Delta z} \tag{2.50}$$

Errors using a PP-type sound intensity probe

When using a PP-type sound intensity probe, the generated intensity error for high frequencies also depends on the finite difference approximation error. The phase mismatch error at low frequencies occurs due to signal propagation delay. The derivation of the errors are given in [29], [30] and an explanation and figures can be found in [31].

For a maximum intensity error of 1 dB the following equation must be true:

$$-1 = 10log\frac{\sin(k\Delta z)}{k\Delta z} \tag{2.51}$$

A graphical solution (figure 2.4) leads to a value of $k\Delta z = 1.15$.

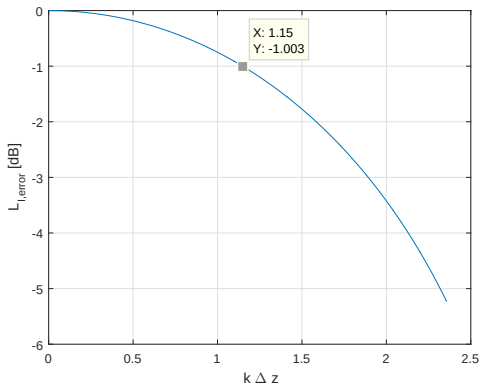

Figure 2.4: High frequency bias intensity error.

The upper frequency limit is then obtained as follows:

$$k\Delta z \leq 1.15 \rightarrow \frac{2\pi f\Delta z}{c} \leq 1.15 \rightarrow f_{I,\max} = \frac{1.15c}{2\pi\Delta z} \approx \frac{c}{6\Delta z} \tag{2.52}$$

From these calculations it follows that $f_{v,\max} = 2f_{I,\max}$.

Jacobsen et al. [32] demonstrated that scattering and diffraction effects are able to cancel the finite difference intensity error.

The lower frequency limit, leading to a maximal intensity error of 1 dB is defined as

$$f_{\min} = \frac{c}{\Delta z}\frac{\mathrm{PM}(f_{\min})}{72^\circ} \tag{2.53}$$

with PM representing the phase mismatch (e.g between $0.1° - 0.3°$).

As a simple rule of thumb, the phase change between the two microphones should be more than five times the phase mismatch for an error within 1 dB [31].

3 Measurements

The following chapter gives some insight into experiments with measured data using the NAH theory, a SONAH implementation and the FD method.

3.1 Measurement Setup

BMW measured the transfer functions of a baffled circular piston with a diameter of 90 mm with a single microphone positioned in 441 positions. The microphone positions have a spacing of 6 mm and capture an area of 120 x 120 mm (see figure 3.1). The measurements are performed in three different layers with a distance of 3, 12 and 24 mm above the piston. For all the calculations, the transfer functions between the measured pressures and a reference signal measured with an accelerometer on the piston are used, assuming a measured piston acceleration of one:

$$H(f) = \frac{S_{ap}}{S_{aa}} = \frac{a^* p}{a^* a} = \frac{a^* p}{|a|^2} \stackrel{!}{=} \frac{p(f)}{a(f)} \stackrel{a(f)=1}{\Longrightarrow} H(f) = p(f) \tag{3.1}$$

U421	U422	U423	U424	U425	U426	U427	U428	U429	U430	U431	U432	U433	U434	U435	U436	U437	U438	U439	U440	U441
U400	U401	U402	U403	U404	U405	U406	U407	U408	U409	U410	U411	U412	U413	U414	U415	U416	U417	U418	U419	U420
U379	U380	U381	U382	U383	U384	U385	U386	ST387	ST388	ST389	ST390	ST391	U392	U393	U394	U395	U396	U397	U398	U399
U358	U359	U360	U361	U362	U363	ST364	ST365	ST366	ST367	ST368	ST369	ST370	ST371	ST372	U373	U374	U375	U376	U377	U378
U337	U338	U339	U340	U341	ST342	ST343	ST344	ST345	ST346	ST347	ST348	ST349	ST350	ST351	ST352	U353	U354	U355	U356	U357
U316	U317	U318	U319	ST320	ST321	ST322	ST323	ST324	ST325	ST326	ST327	ST328	ST329	ST330	ST331	ST332	U333	U334	U335	U336
U295	U296	U297	ST298	ST299	ST300	ST301	ST302	ST303	ST304	ST305	ST306	ST307	ST308	ST309	ST310	ST311	ST312	U313	U314	U315
U274	U275	U276	ST277	ST278	ST279	ST280	ST281	ST282	ST283	ST284	ST285	ST286	ST287	ST288	ST289	ST290	ST291	U292	U293	U294
U253	U254	ST255	ST256	ST257	ST258	ST259	ST260	ST261	ST262	ST263	ST264	ST265	ST266	ST267	ST268	ST269	ST270	ST271	U272	U273
U232	U233	ST234	ST235	ST236	ST237	ST238	ST239	ST240	ST241	ST242	ST243	ST244	ST245	ST246	ST247	ST248	ST249	ST250	U251	U252
U211	U212	ST213	ST214	ST215	ST216	ST217	ST218	ST219	ST220	ST221	ST222	ST223	ST224	ST225	ST226	ST227	ST228	ST229	U230	U231
U190	U191	ST192	ST193	ST194	ST195	ST196	ST197	ST198	ST199	ST200	ST201	ST202	ST203	ST204	ST205	ST206	ST207	ST208	U209	U210
U169	U170	ST171	ST172	ST173	ST174	ST175	ST176	ST177	ST178	ST179	ST180	ST181	ST182	ST183	ST184	ST185	ST186	ST187	U188	U189
U148	U149	U150	ST151	ST152	ST153	ST154	ST155	ST156	ST157	ST158	ST159	ST160	ST161	ST162	ST163	ST164	ST165	U166	U167	U168
U127	U128	U129	ST130	ST131	ST132	ST133	ST134	ST135	ST136	ST137	ST138	ST139	ST140	ST141	ST142	ST143	ST144	U145	U146	U147
U106	U107	U108	U109	ST110	ST111	ST112	ST113	ST114	ST115	ST116	ST117	ST118	ST119	ST120	ST121	ST122	U123	U124	U125	U126
U85	U86	U87	U88	U89	ST90	ST91	ST92	ST93	ST94	ST95	ST96	ST97	ST98	ST99	ST100	U101	U102	U103	U104	U105
U64	U65	U66	U67	U68	U69	ST70	ST71	ST72	ST73	ST74	ST75	ST76	ST77	ST78	U79	U80	U81	U82	U83	U84
U43	U44	U45	U46	U47	U48	U49	U50	ST51	ST52	ST53	ST54	ST55	U56	U57	U58	U59	U60	U61	U62	U63
U22	U23	U24	U25	U26	U27	U28	U29	U30	U31	U32	U33	U34	U35	U36	U37	U38	U39	U40	U41	U42
U1	U2	U3	U4	U5	U6	U7	U8	U9	U10	U11	U12	U13	U14	U15	U16	U17	U18	U19	U20	U21

Figure 3.1: Measurement positioning, ST = piston underneath (yellow), U = no piston underneath.

The measured pressure in the three hologram planes (3, 12 and 24 mm) can be seen in figure 3.2.

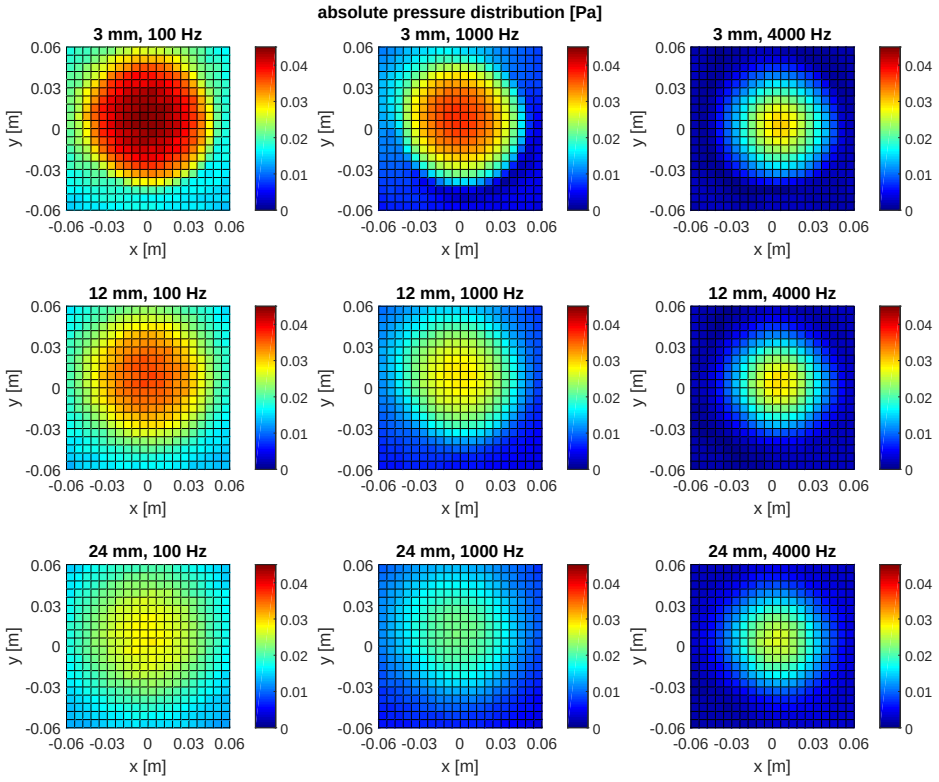

Figure 3.2: Measured pressure distribution above the piston for 100, 1000 and 4000 Hz at at distance of 3, 12 and 24 mm above the piston.

3.2 Measurement Results

In the following section the results of different attempts to determine the pressure and velocity in various layers in z-direction are presented. Firstly, results of forward and backward propagation of the measured pressure values are compared to the real measured pressure values (for NAH and SONAH) to verify if the propagation methodologies work properly. Secondly, the velocity is calculated from the pressure values at a layer and propagated back to the source layer, where the acceleration is known. The velocity at the source can easily be transformed to the source acceleration and compared to the measured source acceleration. This way the effectiveness and precision of the methods can

be examined. For the calibration the calculated velocity is used as a reference and therefore those calculations need to be as accurate as possible.

3.2.1 Testing of Pressure Propagation

Forward Propagation of Pressure Hologram

To test the implementation of NAH and SONAH the sound pressure planes are propagated forward and compared to the measured planes using three different microphone configurations. Firstly, all 21 x 21 measured points are used for the computation (NAH results – figure 3.3, row 2; SONAH results – figure 3.5, row 2). To test the limitations of NAH the measurement area and spacing is reduced. In another step a rectangular configuration (microphone positions inside red square in figure 3.1 – positions above piston) are used for the computations (NAH results – figure 3.3, row 3). Thirdly, only every other microphone of the full array is used leading to 11 x 11 positions with a spacing of a = 12 mm (NAH results – figure 3.3, row 3). For the 21x21 SONAH case unit weighting functions, $\kappa = 1$ and $z^+ = 0$ are used. Figures 3.3 - 3.6 show the results for 100, 1000 and 4000 Hz and propagation from 3 to 12 mm and 3 to 24 mm.

Additionally, a spatially averaged squared error is defined as follows:

$$\epsilon = 10 \cdot \log_{10}\left(\frac{\bar{p^2}}{\bar{p_0^2}}\right), \tag{3.2}$$

where $\bar{p_0^2}$ represents the actual measured pressure at this layer. The results of the error calculations are shown in table 3.1.

		NAH	NAH	NAH	SONAH
f [Hz]	d [mm]	21 x 21	15 x 15	11 x 11	21 x 21
100	$3 \rightarrow 12$	1.25	1.68	1.20	1.26
100	$3 \rightarrow 24$	2.68	3.50	2.58	2.77
1000	$3 \rightarrow 12$	0.96	1.80	0.88	1.07
1000	$3 \rightarrow 24$	2.23	3.67	2.06	2.44
4000	$3 \rightarrow 12$	0.78	1.03	0.79	0.38
4000	$3 \rightarrow 24$	1.26	0.99	1.30	0.95

Table 3.1: Averaged absolute squared error for forward propagation from 3 to 12 mm ($3 \rightarrow 12$) or from 3 to 24 mm ($3 \rightarrow 25$) for different frequencies, microphone configurations and holography implementations.

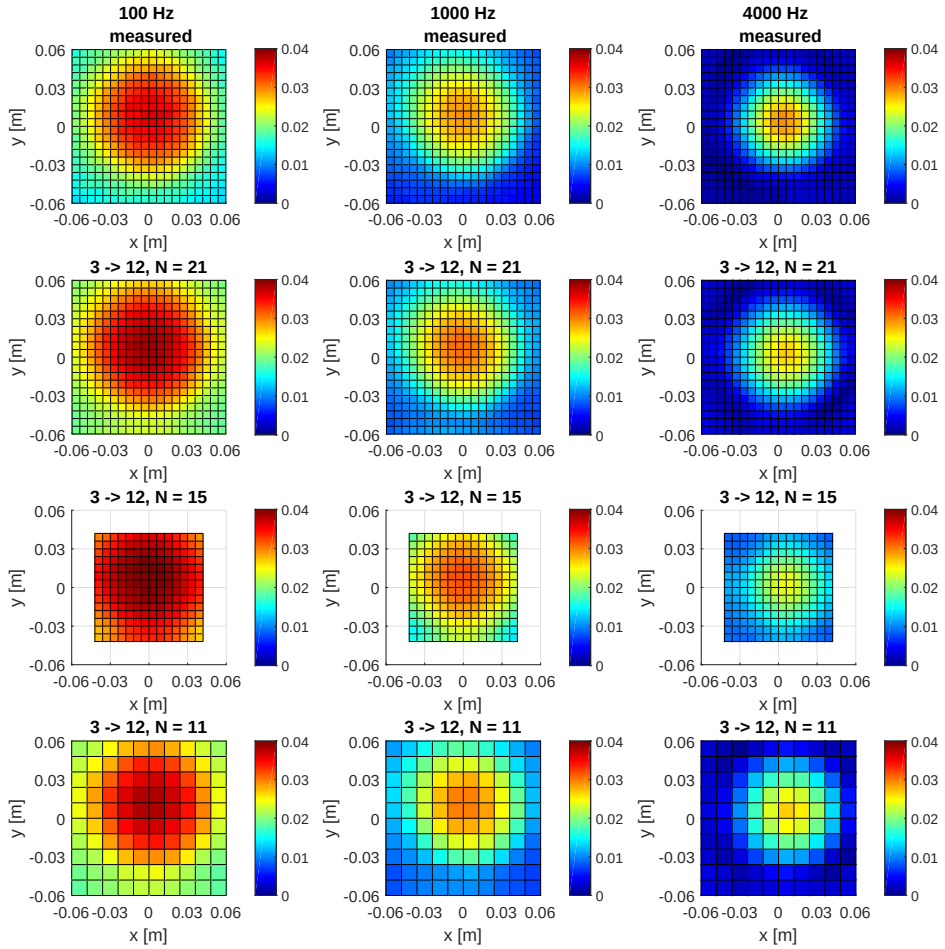

Figure 3.3: Absolute values of the pressure propagated forward from 3 to 12 mm with NAH for 100, 1000 and 4000 Hz; row 1: measured values at 12 mm, row 2 - 4: forward propagation of the measured values at 3 mm to 12 mm, row 4: using all measurement points (N = 21), row 3: using only points above piston (N = 15), row 4: using only every other microphone position (N = 11).

Analysis of the NAH plots (figures 3.3 and 3.4) and the data in table 3.1 leads to the following conclusions:

- The average error $3 \rightarrow 24$ is bigger than the average error $3 \rightarrow 12$.
- The average error decreases with increasing frequency.
- There is no significant difference in the results between N = 21 and N = 11 with same array size (see figure 3.3, rows 2 and 4). This leads to the conclusion that for forward propagation a discrete spacing of 12 mm would be enough.
- If the array only covers the piston area (see figure 3.3, row 3) the error is bigger.

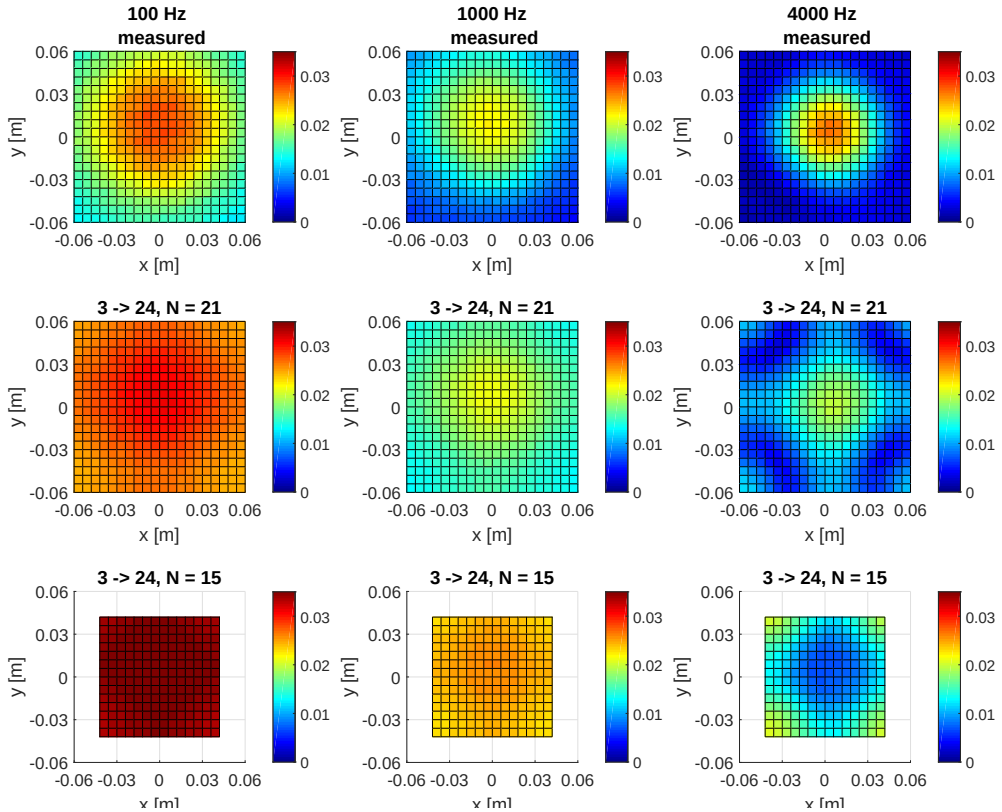

Figure 3.4: Absolute values of the pressure propagated forward from 3 to 24 mm with NAH for 100, 1000 and 4000 Hz; row 1: measured values at 24 mm, rows 2 and 3: forward propagation of the measured values at 3 mm to 24 mm, row 2: using all measurement points (N = 21), row 3: using only points above piston (N = 15).

- For a propagation from 3 to 12 mm at 100 and 1000 Hz NAH overestimates the measured pressure (see figure 3.3, columns 1 and 2). For 4000 Hz NAH underestimates the results (see figure 3.3, column 3).
- At 100 Hz and propagation from 3 to 24 mm at 100 Hz it is hard to identify the shape of the source (see figure 3.4, column 1).
- At 1000 Hz and propagation from 3 to 24 mm the difference between the center and the edges is at least 0.007 Pa and the estimated values above the source correspond to the measured values. Only for the case N = 15 the result is erroneous (see figure 3.4, column 2).
- At 4000 Hz and propagation from 3 to 24 mm the values above the source are underestimated and one can clearly see errors from the Fourier calculations (see figure 3.4, column 3). For N = 11 no appropriate result can be computed and thus, the evaluated absolute squared error in table 3.1 ($\epsilon = 0.99$) cannot be used. However, the maximum frequency for a

microphone spacing $a = 0.006$ should be:

$$f_{max} = \frac{c}{2a} = \frac{343}{2 \cdot 0.006} = 28583\,\text{Hz} \tag{3.3}$$

and for N = 11 and $a = 0.012$

$$f_{max} = \frac{c}{2a} = \frac{343}{2 \cdot 0.012} = 14290\,\text{Hz} \tag{3.4}$$

- If the calculations are repeated for f = 5000 Hz and a propagation from 3 mm to 12 mm as well as to 24 mm is performed, none of the NAH calculations lead to an appropriate result.

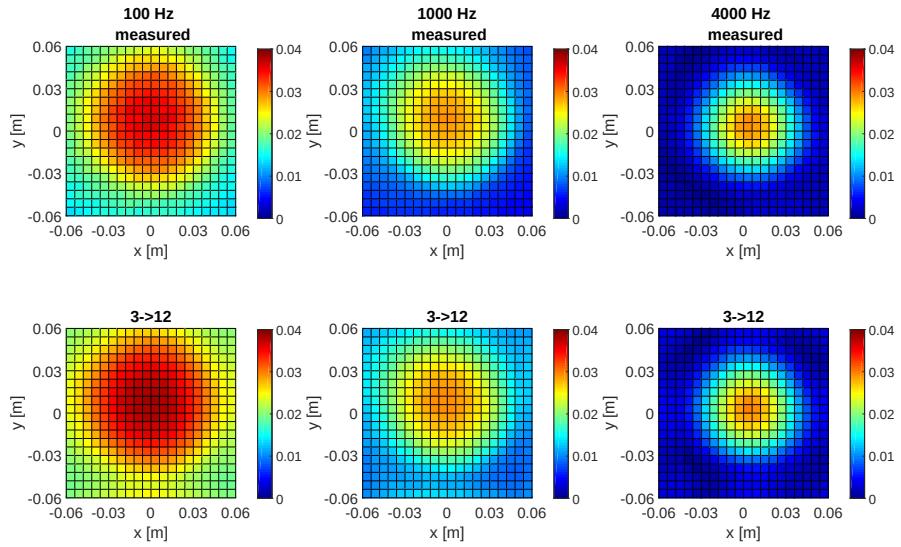

Figure 3.5: Absolute values of the pressure propagated forward from 3 to 12 mm with SONAH for 100, 1000 and 4000 Hz; row 1: measured values at 12 mm, row 2: forward propagation of the measured values at 3 mm to 12 mm using all measurement points.

Analysis of the SONAH plots and the data in table 3.1 leads to the following results:

- The average error $3 \rightarrow 24$ is bigger than the average error $3 \rightarrow 12$.
- The average error decreases with increasing frequency.
- The calculation of the pressure at 12 and 24 mm with the data at 3 mm provides values which are slightly above the measured pressure values at these planes (see figure 3.5 for the 12 mm case). The computation error is reduced with increasing frequency.

- At 100 Hz and for a propagation from 3 to 24 mm the result is erroneous (see figure 3.6).

If the NAH and the SONAH results for 21x21 are compared, the SONAH results are more precise and less prone to errors, because the NAH methodology implies a bigger measurement area than the one used for this measurements. However, SONAH is used within its valid application range, which puts it in advantage.

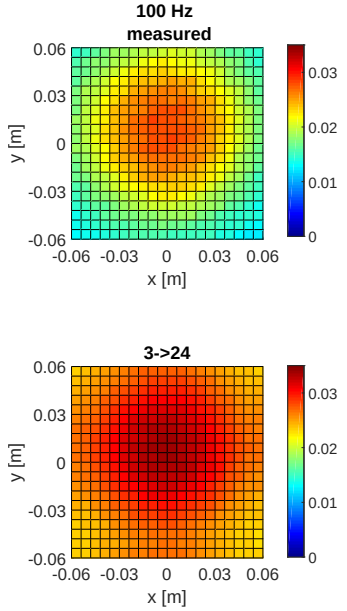

Figure 3.6: Absolute values of the pressure propagated forward from 3 to 24 mm with SONAH for 100 Hz; row 1: measured values at 24 mm, row 2: forward propagation of the measured values at 3 mm to 24 mm using all measurement points.

Backward Propagation of Pressure Hologram

In the next step, it will be analyzed, whether the propagation is also working for the backward pressure case. In this case the matrix H is inverted to get the correct results. The matrix is ill-posed due to measurement noise and calculation errors, resulting from the small measurement aperture, and therefore has to be regularized. This is done with a Tikhonov regularization scheme in combination with General Cross Validation (GVC). Due to the errors which are occurring in the Fourier processing, the regularization sometime does not find a minimum or has its minimum at the smallest α value. If the GCV is not able to find the correct minimum, the inverse H matrix "blows up".

When the standard Tikhonov regularization is used and the smallest absolute diagonal element value of $\mathbf{S}$ ($s_{\min} = \min(\mathrm{diag}(\mathbf{S}))$; see equation 2.17) is set as the minimum value for α ($\alpha_{\min} = |s_{\min}|$), the α values obtained with the GCV scheme are not satisfying at all. The source cannot be localized. If s_{min} times 100 is used as the minimum value for α ($\alpha_{\min} = 100|s_{\min}|$), the GCV has it's minimum at the smallest α. Additionally, the improved Tikhonov regularization scheme is applied. When $\alpha_{\min} = |s_{\min}|$ is used and the measured values at 12 mm are propagated back to 3 mm, the shape of the piston can already be obtained. The values are still noisy and erroneous. Therefore, again $\alpha_{\min} = 100|s_{\min}|$ is used. The propagation from 12 to 3 mm works quite well for the standard regularization (see figure 3.7 a) as well as the improved method (see figure 3.7 b).

For the backward propagation from 24 to 3 mm no usable results were attainable and are therefore not shown in this thesis.

In figure 3.7 d the results with the SONAH implementation for 12 to 3 mm are shown. A unit weighting function, a factor $\kappa = 1$ and a virtual source plane $z^+ = 0$ are used. The calculation of the pressure at the 3 mm plane with the data from the 24 mm plane leads to incorrect results and is therefore not shown in this thesis.

Furthermore, the spatial averaged square error is calculated using equation 3.2. Table 3.2 shows the calculated error.

		NAH	NAH	SONAH
f [Hz]	d [mm]	standard Tikhonov	improved Tikonov	
100	12→3	-1.38	-1.22	-1.47
1000	12→3	-0.36	0.07	-1.11
4000	12→3	0.73	1.00	0.18

Table 3.2: Averaged absolute squared error for backward propagation from 12 to 3 mm ($12 \rightarrow 3$) for different frequencies, microphone configurations, regularization methods and holography implementations.

Evaluation of the error in table 3.2 and of figure 3.7 leads to the following results:

- The error values are insignificant. They only show a spatial average.
- For NAH and SONAH only the 12 to 3 mm propagation case leads to an appropriate result (see figure 3.7 b - d). In the 24 to 3 mm propagation case the matrix is ill-conditioned, it cannot be regularized properly with $\alpha_{min} = 100|s_{min}|$ and therefore, the errors in the result diverge.
- The GCV cannot manage to find a usable α value.

- The quality of the shape estimate depends on the minimum value of α.
- The standard and the improved Tikhonov regularization with $\alpha_{min} = \alpha_{reg} = 100|s_{min}|$ lead to similar results with a slight underestimation compared to the measured values (see figure 3.7 b and c).
- The regularization in the SONAH scheme leads to appropriate results as well (see figure 3.7 c).

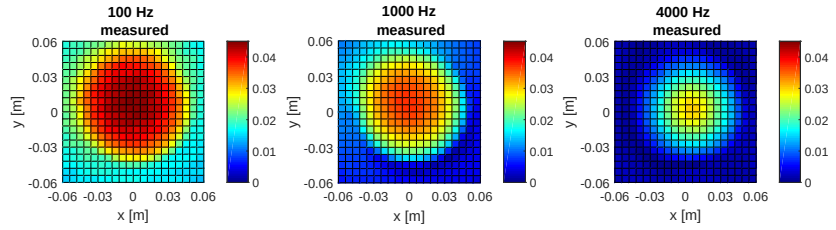

(a) measured values at 3 mm

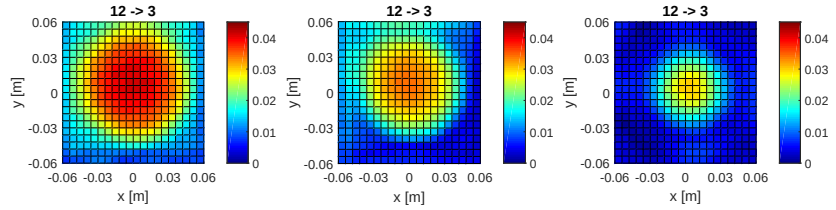

(b) Propagated values using NAH, standard Tikhonov regularization and $\alpha_{\text{min}} = 100|s_{\text{min}}|$

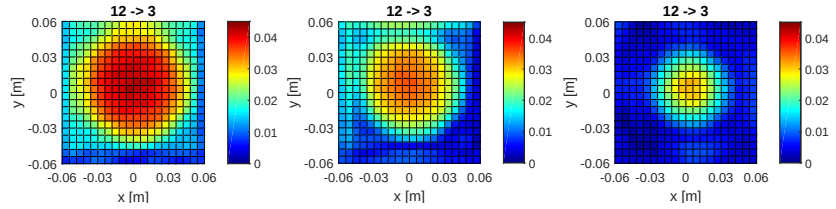

(c) Propagated values using NAH, improved Tikhonov regularization and $\alpha_{\text{min}} = 100|s_{\text{min}}|$

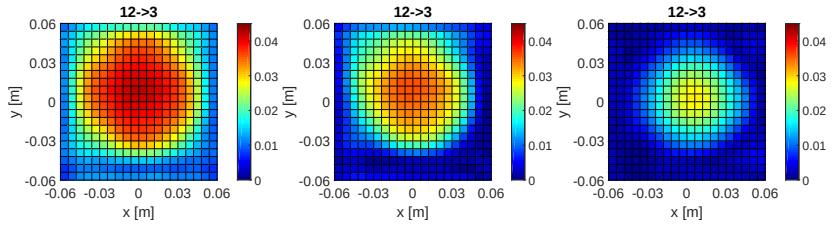

(d) Propagated values using SONAH, a unit weighting function, factor $\kappa = 1$ and virtual source plane $z^+ = 0$

Figure 3.7: Absolute values of the pressure propagated backward from 12 to 3 mm for 100 (column 1), 1000 (column 2) and 4000 Hz (column 3) using all measurement positions.

Angular Spectra

For a better understanding of the occuring error, the angular spectrum for the NAH case is analyzed. According to [14, p. 33], the plane waves only undergo phase changes. So for $k_x = k_y = 0$ and $k_z = k$ the angular spectrum becomes $P(0,0)e^{ikz} = P(0,0)e^{ik_z z} = P(0,0,z)$. But when one has a look at figure 3.8 a, one sees that there is also a change in the measured absolute pressure values for 3 and 12 mm (figure 3.8 a row 1) at position $k_x = k_y = 0$. This leads to the error, which is caused e.g. in the forward propagation from 3 to 12 mm (figure 3.8 a, row 2).

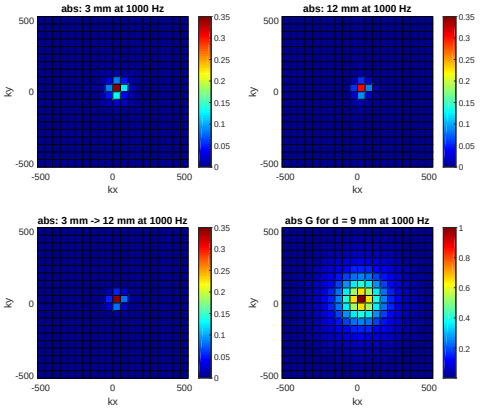

(a) Absolute values

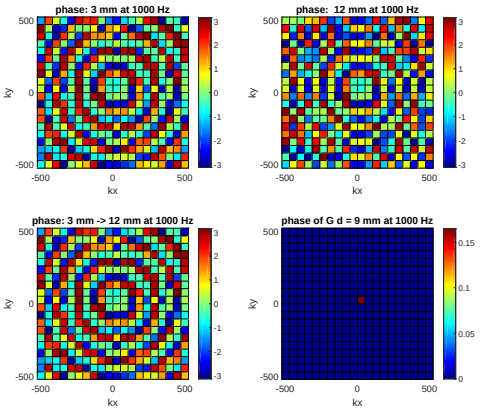

(b) Phase

Figure 3.8: Absolute values and phase of the angular spectrum at 1000 Hz; row 1 and column 1: measured values at 3 mm, row 1 and column 2: measured values at 12 mm; row 2 and column 1: propagated values from 3 to 12 mm; row 2 and column 2: propagation factor G for a distance of 9 mm.

3.2.2 Velocity Calculation

The main target of this thesis is to calculate a velocity with the help of measured pressure data and use this velocity as a reference for calibration. In the next step the velocity at the source position is calculated to examine how precise the methodologies are. To verify the correctness of the calculated velocity, the acceleration is computed by multiplying the received velocity with $i \cdot \omega$. Comparing to equation 3.1 an acceleration value of 1 should be obtained on the whole piston.

When using the improved Tikhonov regularization scheme in the NAH case the shape of the piston cannot be obtained. The result is inaccurate, mostly random and not plotted in this thesis. The best results for the piston acceleration are generated by using the pressure values from the 3 mm plane. Scaling and accuracy of the absolute acceleration values depend on the regularization factor α of the standard Tikhonov regularization. Figure 3.9 shows the result for $\alpha_{\text{min}} = \alpha_{\text{reg}} = 100|s_{\text{min}}|$ with an assumed measurement distance of 3 mm, which is identical to the distance from the source to the protective grid of the microphone transducer. The distance of 4.5 mm in figure 3.10 is equal to the distance from the source to the membrane of the microphone. The errors are regularized properly, but thereby also the acceleration value is diminished. Furthermore, due to the strong regularization the acceleration values over the area of the piston are not equal. They get smaller at the edges, similar to the shape of a parabola. If $\alpha_{\text{min}} = \alpha_{\text{reg}}$ is smaller, then the acceleration value gets bigger, but more errors occur as well. E.g. for $\alpha_{\text{min}} = \alpha_{\text{reg}} = |s_{\text{min}}|$ the shape of the piston cannot be obtained.

The SONAH acceleration calculation is performed with a velocity scaling function, κ = 1, $z^+ = 0$ and d = 3 mm. Again the used regularization is able to find an appropriate minimum. Acceleration values are more or less the same on the whole piston for 100 and 1000 Hz. For 4000 Hz again a parabola shape is obtained. The piston acceleration values for 100 Hz are smaller than 1, for 1000 Hz around 1 and for 4000 Hz bigger than 1, or more precisely even bigger than the color bar scaling with values up to 2.12.

In both the NAH and SONAH calculations a significant drop in the acceleration value at the rim of the piston can be seen. This is due to a small gap between the piston and the baffle.

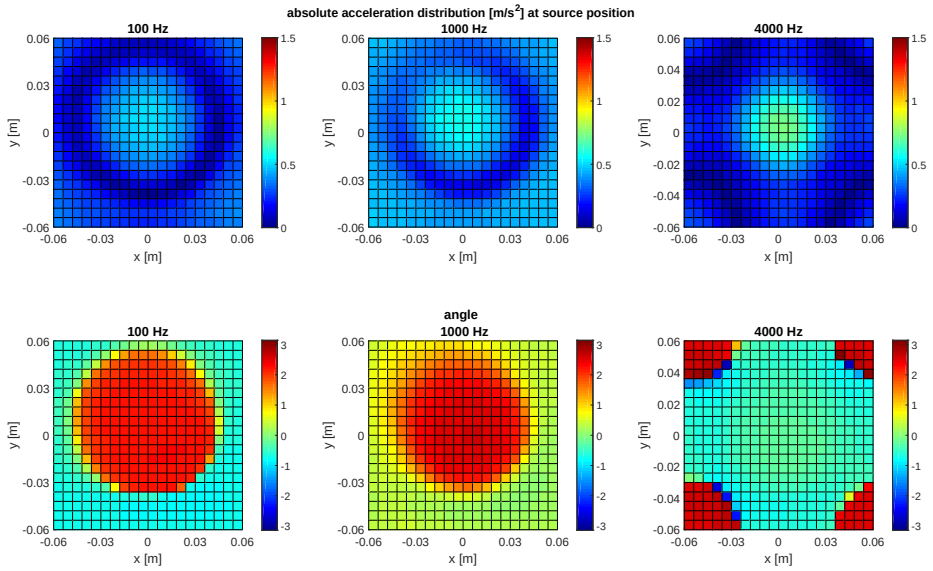

Figure 3.9: Source acceleration using d = 3 mm with NAH for $\alpha_{\min} = \alpha_{\text{reg}} = 100|s_{\min}|$; row 1: absolute values [m/s^2], row 2: phase [rad].

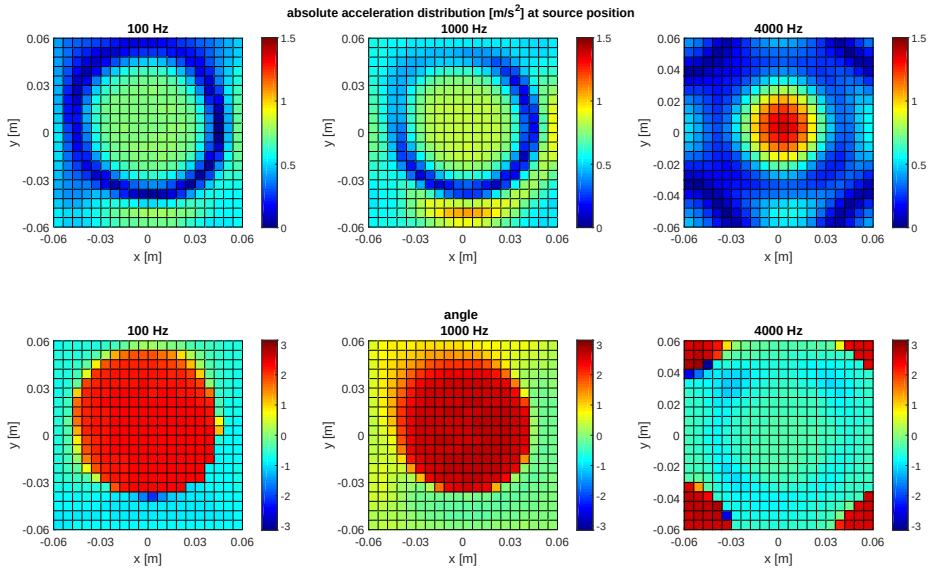

Figure 3.10: Source acceleration using d = 4.5 mm with NAH for $\alpha_{\min} = \alpha_{\text{reg}} = 100|s_{\min}|$; row 1: absolute values [m/s^2], row 2: phase [rad].

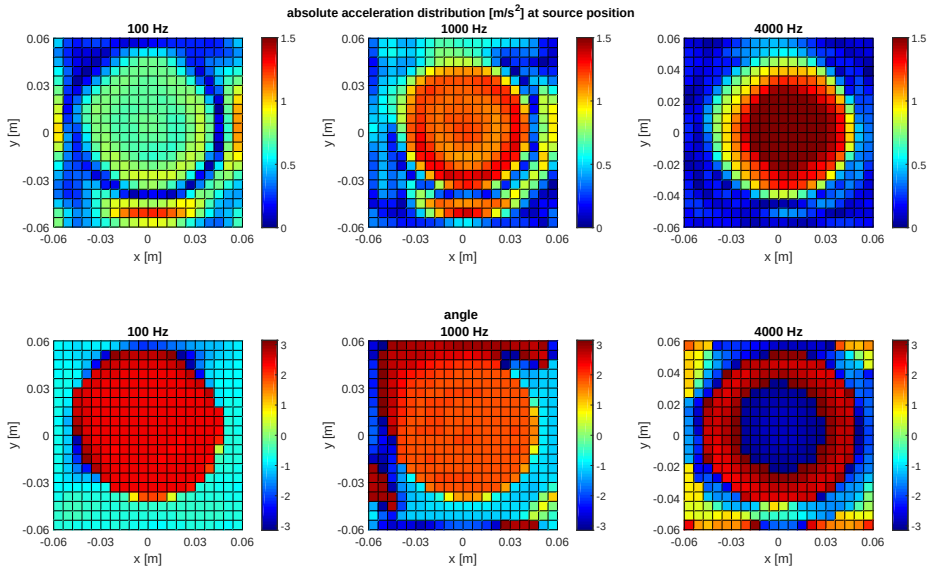

Figure 3.11: Source acceleration using d = 3 mm with SONAH, velocity scaling function and $\kappa = 1$; row 1: absolute values [m/s^2], row 2: phase [rad].

With FD it is not possible to calculate back to the source, so the verification of an acceleration of 1 is not feasible. It is possible to compute the acceleration in the middle of two measurement points. Figure 3.12 shows the calculation results for 7.5/9 mm, 13.5/15 mm, 18/19.5 mm, using the protective grid or the microphone membrane itself as distance reference. For 100 and 1000 Hz the calculated values are reasonable with decreasing values for an increasing distance. However, for 4000 Hz the values increase with increasing distance. The maximum frequency for the FD scheme is calculated using equation 2.52:

$$f_{\max} = \frac{c}{6\Delta z} \tag{3.5}$$

$$f_{\max,13.5/15} = \frac{343}{6 \cdot 0.021} = 2722\,\text{Hz} \tag{3.6}$$

$$f_{\max,18/19.5} = \frac{343}{6 \cdot 0.012} = 4764\,\text{Hz} \tag{3.7}$$

The calculation shows that for 4000 Hz using the 3 and 24 mm planes, the achievement of a correct result is not guaranteed and when the 12 and 24 mm planes are used, 4000 Hz is near the maximum limit of 4764 Hz. Thus, the calculation also could be critical.

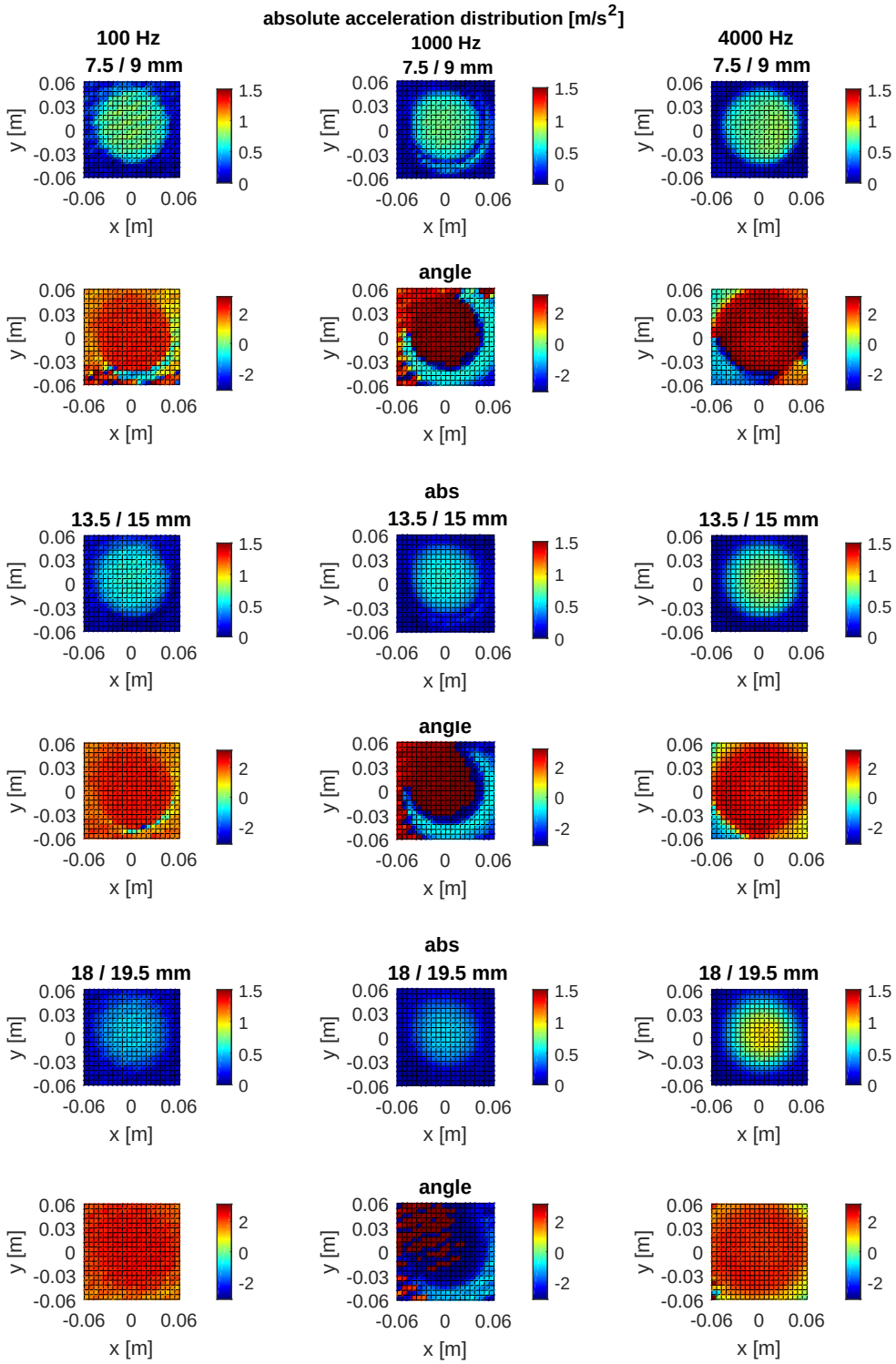

Figure 3.12: Acceleration values obtained with FD; rows 1, 3 and 5: absolute values [m/s^2], rows 2, 4 and 6: phase [rad].

3.3 Summary of the Measurement Results

The outcome of the experiments is not satisfactory, although the forward propagation leads to appropriate results when the distance is small enough and the frequency is underneath 4000/5000 Hz. The backward propagation of sound pressure and particle velocity is error-prone. The GCV in combination with NAH always determines the smallest α value as regularization parameter. This leads to a hand tuning of the parameter, which should not be the case if a GCV scheme is used. If an α value is found which is able to reconstruct the piston shape, the obtained particle velocity and acceleration is damped heavily, again leading to errors. With the SONAH implementation, the accuracy of the results depends on the choice of scaling function, the value κ and the position of the virtual source plane z^+. Especially the acceleration results show a strong frequency dependence.

One problem in NAH is the pressure discontinuity at the end of the measurement aperture. For a proper use of the Fourier transform, the pressure at the ends must be zero. In this case this is not true and therefore the discontinuity represents a space region with many high wavenumbers, which leads to a level blow up after the inversion. In literature (e.g.[22]) the method of border padding is introduced. The methodology is explained in the theory error section and tries to reduce the generated errors.

In the implementation for this thesis every other measurement point is used, ending up with 11 points in x-direction and 11 points in y-direction. In the next step 15 samples are added at the edges of the array leading to 41 points in x- and 41 points in y-direction. Finally, the new array data is processed by the NAH algorithm, standard Tikhonov regularization and GCV. Unfortunately, the GCV again has it's minimum at the smallest α value, so one ends up with the same problem of finding the correct regularization value. This is due to the fact that border padding introduces an unreal and artificial field outside of the array edges, which leads to a wrong near field and errors. Figure 3.13 shows the result for $\alpha_{\text{min}} = \alpha_{\text{reg}} = |s_{\text{min}}|$ using a distance of 3 mm. If a measurement distance of 4.5 mm is assumed the receive source velocity values are slightly bigger. By increasing the $\alpha_{\text{min}} = \alpha_{\text{reg}}$ value, the result is more damped and a parabola form would appear.

Williams et al. [33], as well as Zhang et al. [34], propose the use of a so called Patch Near Field Acoustical Holography to continue the pressure field outside the measurement area, based on the measured field. When applying the theory from these papers to reconstruct the pressure values outside the measured area, the results do not improve. This is mainly due to the fact, that the aperture

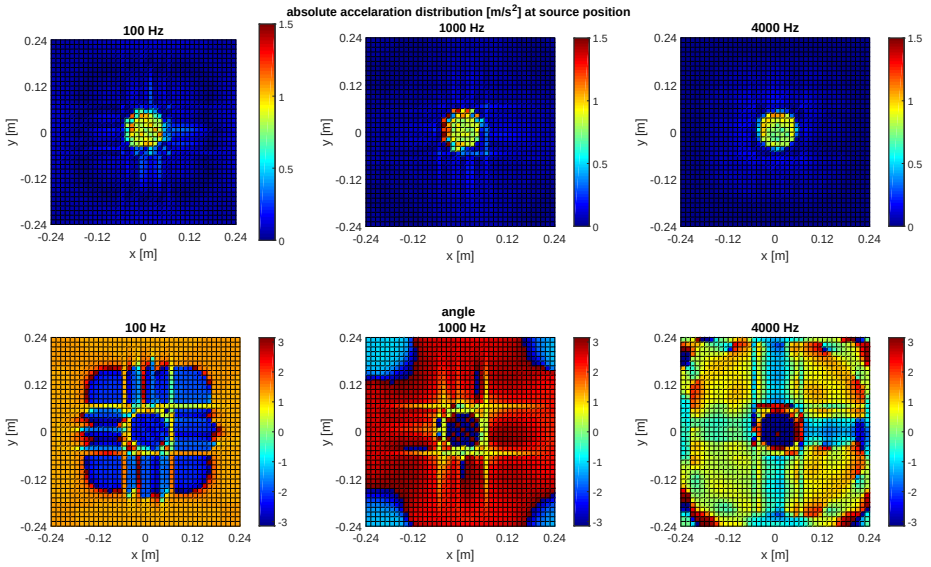

Figure 3.13: Source acceleration using d = 3 mm, NAH and border padding.

already covers the complete source area and in theory a patch much smaller than the source is considered.

If one of the particle velocity values obtained with NAH, SONAH and FD has to be used as a reference velocity for calibration, the use of the FD results is recommended. They seem to be stable and less prone to errors due to too small measurement arrays and Fourier calculations (as in NAH) or the use of the correct scaling function and positioning of the virtual source plan (as in SONAH).

4 Simulations

4.1 Simulation Setup

The array used for the experiments in section 3 is too small to obtain satisfactory results. Therefore, the propagation of the sound field in a bigger area above a piston is simulated.

To be able to do the calculations and the regularization properly, Williams [15] required that the pressure at the measurement aperture's edges is at least 30 dB lower compared to the maximum value. The simulations show that 20 dB are enough. The simulated piston has a diameter of 9 cm and the aperture is 40 cm wide with 41 simulated points in x- and y-direction. This leads to a spacing a of 1 cm. 41 points are used, because experiments with a higher number of sampling points in space show better results. In the holography cases the wavenumber components k_x and k_y are sampled with a higher rate and higher values are allowed. For the given measurement grid the maximum frequency is

$$f_{\max} = \frac{c}{2a} = \frac{343}{2 \cdot 0.01} = 17150\,\mathrm{Hz}, \tag{4.1}$$

leading to a maximum wave number of

$$k_{\max} = \frac{\pi}{a} = \frac{\pi}{0.01} = 314.16\,\mathrm{m}^{-1} \tag{4.2}$$

The pressure distribution is calculated in 3 planes which have a distance d of 1 mm, 3 mm and 12 mm. The last two have the same distance as measured by BMW for comparison purposes. The 1 mm plane is simulated for FD purposes.

The simulated piston has a square shape and the sound pressure at the simulated measurement planes is obtained using the Rayleigh's first integral formula in a discretized version. One must be aware that the discretization of the integral and the truncation could cause errors. Various simulation attempts show that in order to get correct FD and NAH results, the discretization step of the integral must be fine enough. For the results presented here, the discretization has a spacing of 1 mm ending up with 91 x 91 in phase monopoles. An explanation,

why so many point sources are needed, could be that for point sources the distance to the measurement system is crucial. The closer the array is positioned to a point source, the higher the spatial variation. Higher frequency components are obtained, which could potentially violate the sampling theorem [35].

The simulated pressure values for 100, 1000 and 4000 Hz are plotted in figure 4.1. At 100 and 1000 Hz the on axis pressure value diminishes with increasing distance, but at 4000 Hz the pressure increases with increasing distance. This error could be due to the fact that the sampling rate of the discretization is still too small.

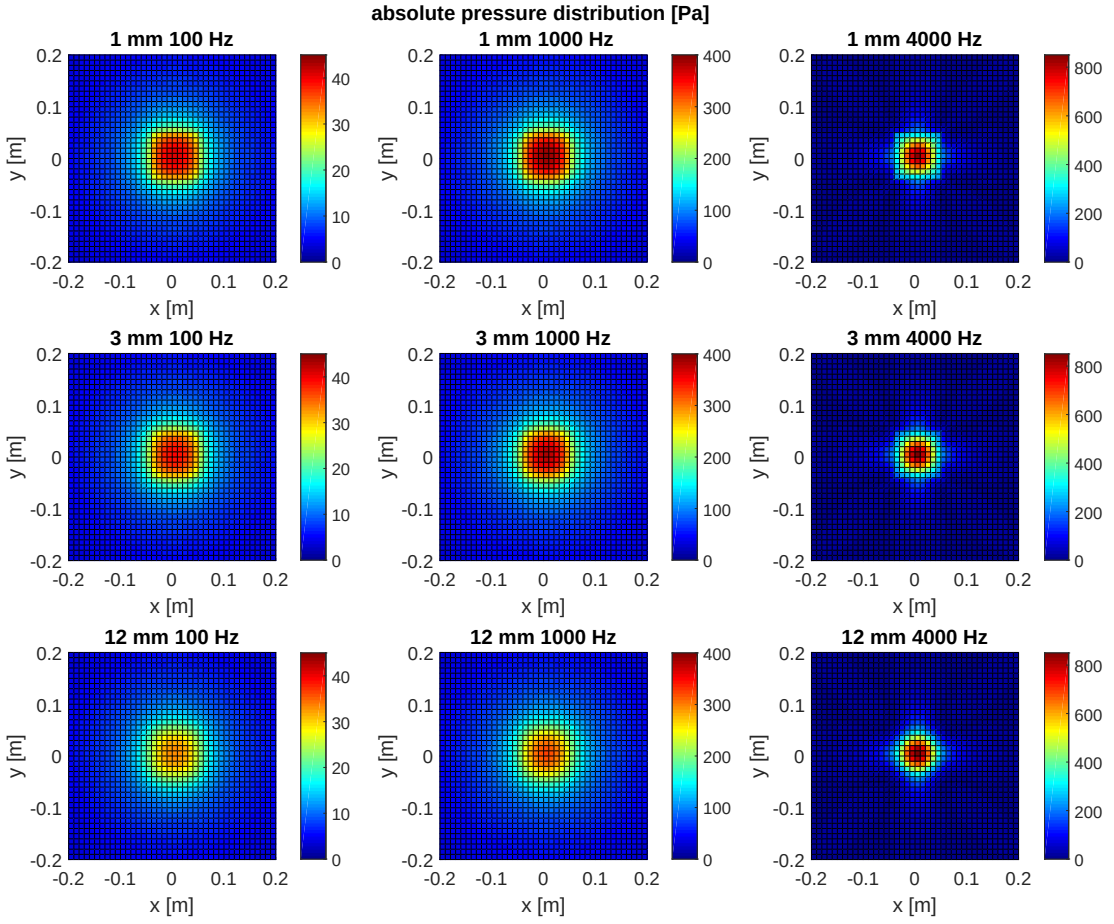

Figure 4.1: Simulated pressure distribution above the piston for 100, 1000 and 4000 Hz at at distance of 1, 3 and 12 mm above the piston assuming a piston velocity of one.

4.2 Simulation without Noise

For a quality examination of the different calculation methods, the simulated data is used without noise corruption. Therefore, the matrix inversion in the NAH and SONAH implantation is the pseudoinverse and no regularization method is applied. The results are plotted and described on the next pages.

4.2.1 Testing of Pressure Propagation

As a first step, the pressure is backpropagated towards the source and is compared to the simulated pressure in this layer. Figure 4.2 shows the backward propagation from the 12 mm plane to the 3 mm plane, where it is compared to the the simulation at 3 mm. The differences are smaller than 1%. From this, one can conclude that the NAH implementation works properly for pressure propagation.

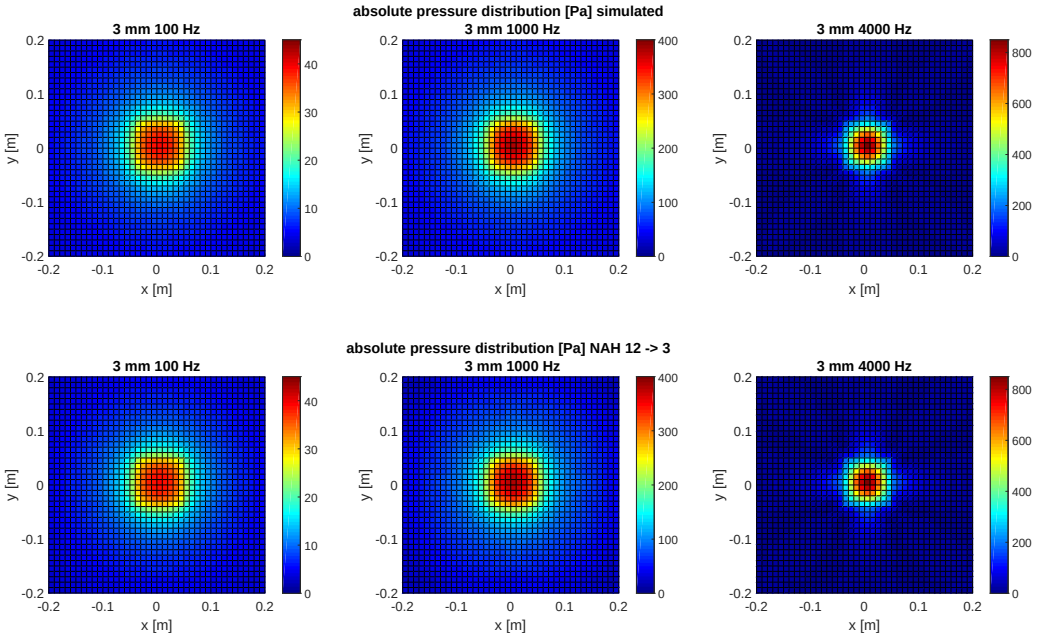

Figure 4.2: Absolute values of the pressure propagated backward from 12 to 3 mm for 100 (column 1), 1000 (column 2) and 4000 Hz (column 3) using NAH, row 1: simulated values at 3 mm, row 2: propagated values.

4.2.2 Velocity Calculation

In the simulation of the pressure, monopoles with a velocity value of one are used. So this velocity value shall be obtained when it is recalculated at the source position with an appropriate velocity propagator and measured pressure data.

In order to compare the results also with FD the pressure data at 12 mm is used for a velocity calculation at 7.5 mm with the NAH and SONAH implementation. The FD results in this plane are computed with the pressure simulation in the 3 mm and 12 mm layer. For SONAH, the velocity scaling function, $\kappa = 1$ and $z^+ = 0$ are used. The results are plotted in figure 4.3.

For 100 Hz the NAH, SONAH and FD absolute values are the same with an error smaller than 1% between each other (see figure 4.3, row 1).

At 1000 Hz the NAH and FD computations provide results above the piston, which differ by 2%. The SONAH implementation result for 1000 Hz already differs from the other results mainly due to the regularization which dampens a lot of useful values and reduces the shape (see figure 4.3, row 3).

At 4000 Hz every implementation results in different values. A reason for this is the simulated pressure distribution at high frequencies. E.g. the SONAH result for x = y = 0 is bigger than the maximum color-bar value ($2.245 > 1.5$). Additionally, the FD results in a value bigger than 1 which is unexpected. These errors result from the simulated pressure propagation at 4000 Hz, where the pressure increases. Therefore, the values at 12 mm are bigger than the values at 3 mm and this could cause the errors.

Next, the phase is analyzed (see figure 4.3, row 2, 4 and 6 for 100, 1000 and 4000 Hz respectively). The NAH and FD phases above the piston at 100 and 1000 Hz have a value of approximately 0 and for SONAH approximately $\frac{\pi}{2}$ for 100 Hz and approximately 1.1 at 1000 Hz. This may be due to an implementation error in the phase term. At 4000 Hz the NAH and FD angle above the piston have a maximum value of 0.57 rad. A closer look at the wavelength of 4000 Hz reveals a value of 0.0858 m:

$$\lambda = \frac{c}{f} = \frac{343}{4000} = 0.0858\,\mathrm{m} \tag{4.3}$$

Therefore, at the position of the calculated velocity at 7.5 mm, the wave has propagated already 10 % of its wavelength. By assuming a total phase change of 2π for a whole wavelength, 10 % equals 0.63 rad. The calculated value of 0.57 rad is quite close to this theoretical value.

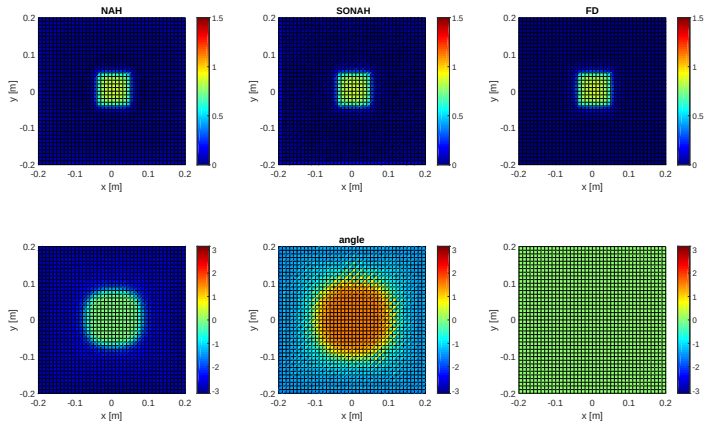

(a) 100 Hz

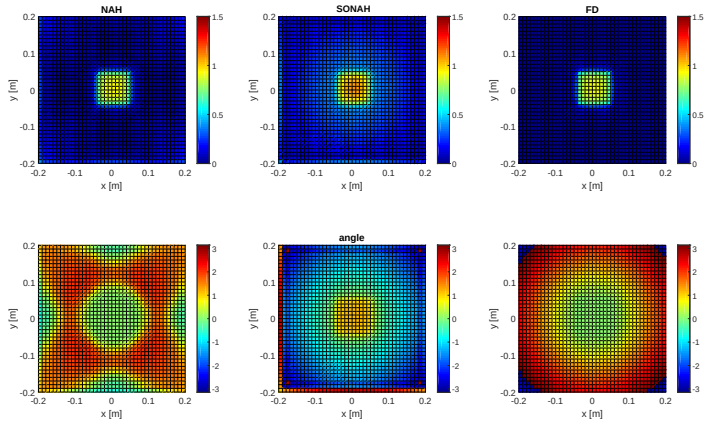

(b) 1000 Hz

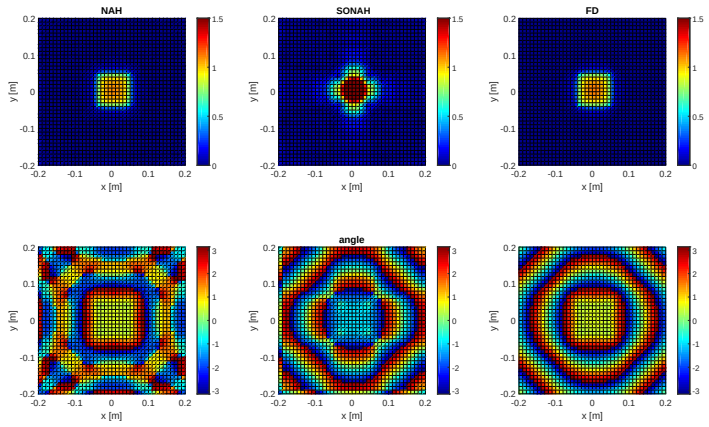

(c) 4000 Hz

Figure 4.3: Absolute values (rows 1, 3, 5) and phase (rows 2, 4, 6) of the velocity using NAH and backward propagation from 12 to 7.5 mm (column 1), SONAH and backward propagation from 12 to 3 mm (column 2) as well as FD using values of layers at 3 and 12 mm.

Furthermore, the velocity is calculated at 2 mm out of the 3 mm data with NAH and SONAH and compared with FD which uses the data at 1 mm and 3 mm. As in the 7.5 mm case, the absolute values at 100 Hz are the same for all implementations. At 1000 Hz the difference between the NAH and FD is approximately 3% and at 4000 Hz the results are erroneous, mainly due to the simulation error. All phase results for NAH and FD above the piston approach zero. The SONAH calculations show the same effect as in the 7.5 mm case. Since the conclusion of this calculation is comparable to the outcome of the calculation at 7.5 mm the results are not plotted.

One noteworthy result is the FD phase calculation at 100 Hz and 7.5 mm as well as 2 mm. It provides a value of zero over the whole simulated area. This results from the small phase change between the two simulated microphone planes. The phase change according to the distance can be calculated with the formula

$$\frac{\Delta z \cdot 360^\circ}{\lambda}, \tag{4.4}$$

with $\lambda = 3.43$ m for 100 Hz, leading to a phase change of 0.79° for a distance of 7.5 mm and 0.21° for a distance of 2 mm. Both values are much smaller than five times the phase mismatch due to a time delay between the two measurement channels of 0.3° ($5 \cdot 0.3^\circ = 1.5^\circ$).

Velocity of the Piston

As a last step, the velocity of the piston is calculated by using the simulated pressure values at 3 mm. An absolute value of one, a phase of zero and a rectangular piston shape is expected. The results are plotted in figure 4.4 for NAH and SONAH for all three simulated frequencies.

SONAH delivers good absolute values at 100 Hz, but at 1000 Hz the obtained results are too big and at 4000 Hz the rectangular piston shape cannot be extracted from the plot.

NAH reconstructs the piston very precisely for all three frequencies, but the values at the rims are slightly higher compared to the other piston values. This results from the rectangular piston shape and is known as Gibbs phenomenon in Fourier series expansion. The sharp edges result in high k-values. The rectangle transforms to a sinc function in k-space which ends abruptly at the ends. It can be corrected e.g. with a windowing function in frequency or k-space domain or with a Padé approximation.

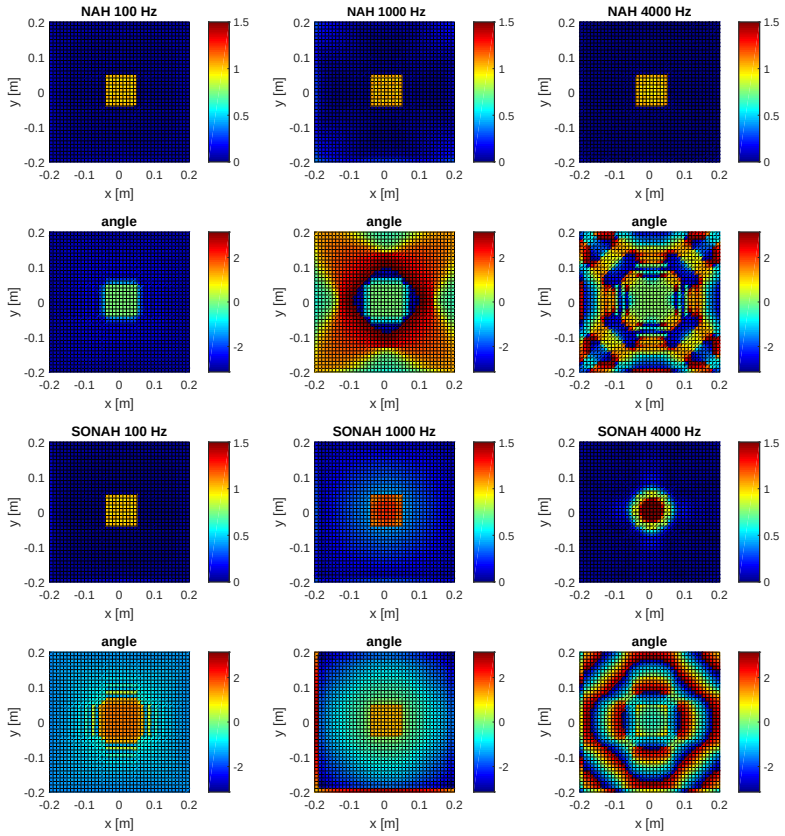

Figure 4.4: Source velocity caluclated with NAH (rows 1 and 2) and SONAH (rows 3 and 4) for 100 (column 1), 1000 (column 2) and 4000 Hz (column 3); rows 1 and 3: absolute values [m/s], rows 2 and 4: phase [rad].

4.3 Simulation with Noise

For an examination of the quality of the different calculation methods, the simulated data is used without noise corruption. A SNR value of 50 dB is simulated with the following equations:

$$\text{noisefactor} = \frac{1}{10^{\frac{\text{SNR}}{20}}} \tag{4.5}$$

$$\text{noise} = 2(\text{rand}(N) - 0.5) \tag{4.6}$$

The noisefactor is multiplied with the maximum real and imaginary part from the 12 mm plane and with random numbers between -1 and 1 (different values for real and imaginary part). This factor is then added to the simulated real and imaginary pressure values. The random numbers differ for every layer and for both, real and imaginary part.

The results are plotted and described on the next pages.

4.3.1 Testing of Pressure Propagation

As in the noisefree case, the pressure from 12 mm is propagated backwards to 3 mm. The standard Tikhonov regularization works fine and the propagated values are the same as the simulated ones (see figure 4.5).

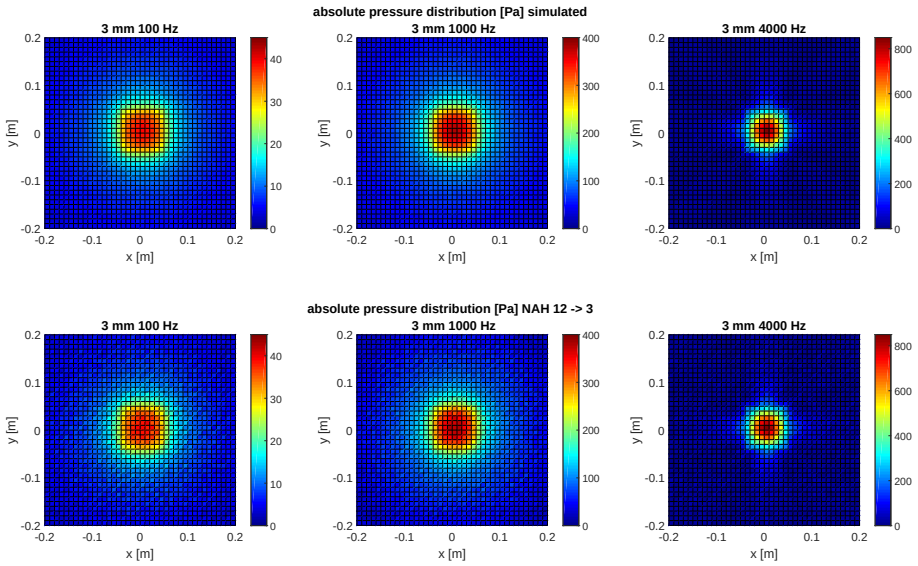

Figure 4.5: Absolute pressure values at 3 mm; row 1: simulated values, row 2: backward propagation of the simulated values at 12 mm to 3 mm using NAH.

4.3.2 Velocity Calculation

As in the noiseless case, the velocity is calculated at distance layers of 7.5 and 2 mm and at the source positions. The results for the velocity calculation at 7.5 mm are plotted in figure 4.6 and for the obtained velocity at source position in figure 4.7. The added noise can clearly be seen in the plots, especially

at positions outside the piston. In NAH and SONAH the inverse matrices are properly regularized with standard Tikhonov regularization and SVD or eigenvalue decomposition, respectively.

The NAH results are good for all calculated frequencies and distances and are comparable to the results obtained with FD. Unfortunately, for the source velocity case and 4000 Hz the SVD does not converge and therefore no result is presented. The angle is zero or at least close to zero for the propagation to the source position and for a distance of 2 and 7.5 mm and low frequencies. The amplitudes at the source position have a value of approximately 1 in the NAH case.

As in the noiseless case, the amplitudes obtained with SONAH are appropriate for 100 Hz, slightly too high for 1000 Hz and for 4000 Hz the shape is wrong and the values are too high. The obtained angle with SONAH is always shifted with a factor of $\frac{\pi}{2}$.

In the FD plots the noise can be clearly seen especially outside the piston.

4.4 Summary of the Simulation Results

The simulations show that it is possible to compute back to the array and to obtain the correct particle velocity for the NAH case. This is due to the fact that the simulated measurement array is much bigger than the simulated piston. The SONAH implementation causes wrong amplitudes and a smaller circular shape. This could be due to the used velocity scaling or due to the fact that the matrix is ill-conditioned although there is no noise added. Maybe it is possible to obtain better SONAH results if a regularized inverted matrix is used in the noiseless case as well. Furthermore, the amplitude values are too high and the phase value is shifted in the noise case as well. Consequently, the use of SONAH for particle velocity calibration is not recommended, at least not for the implementation used in this thesis, which uses a finite number of basic functions. Very similar values are achieved when comparing the NAH solutions with the FD results.

The simulation with noise shows that the GCV in combination with the Tikhonov approach is able to regularize an ill-conditioned matrix properly and that the values obtained with NAH could be used for the calibration of velocity sensors, if the measurement area is big enough. Although, if one wants to ISO standardize the calibration procedure, the documentation of computations and measurements performed and time requirement for NAH is much larger compared to FD, because holography needs much more measurement positions. Therefore, the focus lies on FD for the rest of the thesis.

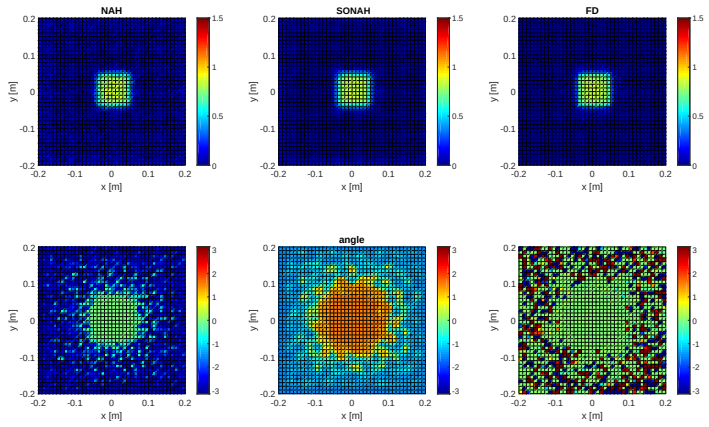

(a) 100 Hz

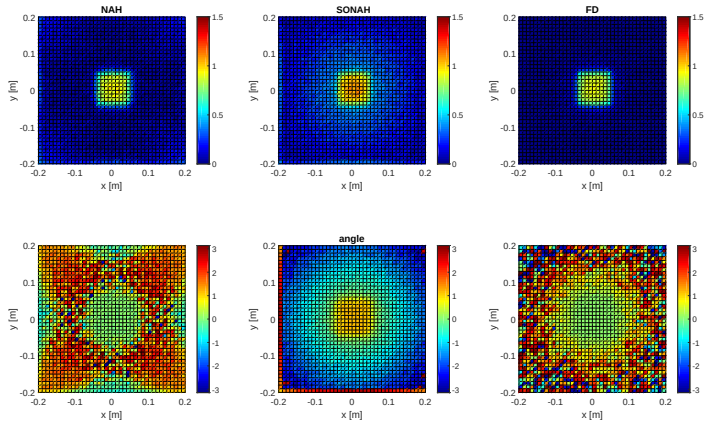

(b) 1000 Hz

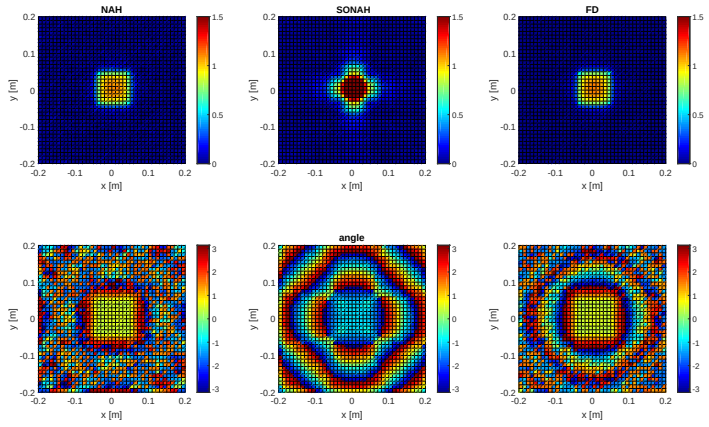

(c) 4000 Hz

Figure 4.6: Absolute values (rows 1, 3, 5) and phase (rows 2, 4, 6) of the velocity using NAH and backward propagation from 12 to 7.5 mm (column 1), SONAH and backward propagation from 12 to 3 mm (column 2) as well as FD using values of layers at 3 and 12 mm corrupted with noise.

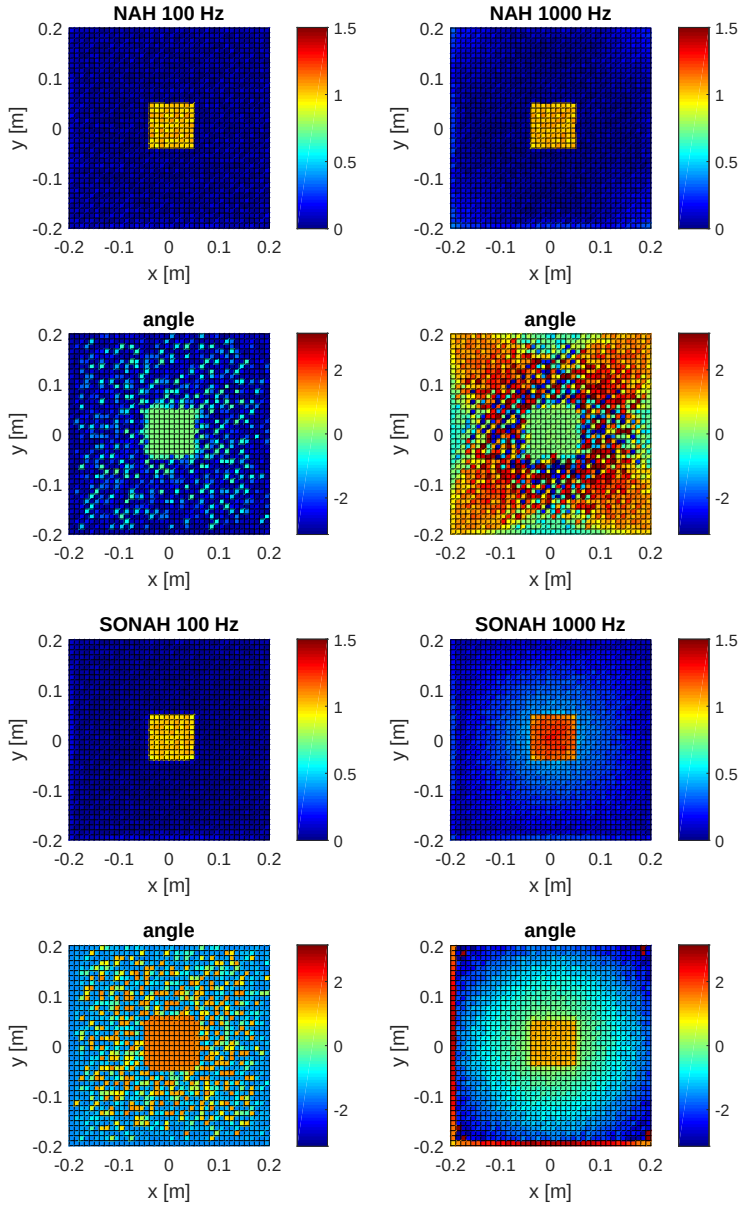

Figure 4.7: Source velocity caluclated with NAH (rows 1 and 2) and SONAH (rows 3 and 4) for 100 (column 1) and 4000 Hz (column 2); rows 1 and 3: absolute values [m/s], rows 2 and 4: phase [rad].

5 Finite Difference Experiments

The last sections have shown that the results obtained with FD are satisfactory and for a calibration procedure fewer pressure measurement points are needed compared to holography. Therefore, as a final step in this thesis, measurements using the Tbox with its baffled square piston as exciter are conducted. The aim is to use FD to find a stable vectorial sound field where the velocity sensor can be calibrated and the influence of position errors is minimized.

5.1 Measurement Setup

A sketch of the Tbox can be found in figure 1.1. The 20x20 cm squared piston of the Tbox in combination with a shaker (Brüel and Kjær vibration exciter type 4809) is used to excite the sound field. With the help of a piezoelectric charge accelerometer (Brüel and Kjær type 4384) and a charge amplifier (Brüel and Kjær type 2635) the acceleration and thereby the velocity of the piston are measured as reference.

The pressure field above the piston is scanned in 11 layers (with a distance of 5 mm up to 55 mm between the piston and the membrane of the microphone with a spacing of 5 mm). In every layer 49 measurement positions with a spacing of 5 mm cover a region of $\pm$ 15 mm compared to the center of the piston (see figure 5.1). Every position is measured with the same microphone, a G.R.A.S. 46AE 1/2" ICP free-field microphone. Furthermore, the velocity is measured with a Microflown PU Mini probe in approximately 50 positions in the different layers above the center of the piston and slightly off-centered ($\pm$ 5 mm in x- and y-direction). The positioning of the microphone and the velocity sensor is done with the help of a positioning system, which is able to move in mm steps in three coordinates (see figure 5.2).

With an LMS system a continuous random white noise in a frequency range of 50 Hz up to 10000 Hz with a level of 5 V is generated and used as excitation signal. The frequency response functions between the pressure (or velocity) and the reference acceleration are computed (see equation 3.1) and 100 averages are performed. A frequency resolution of 5 Hz is used.

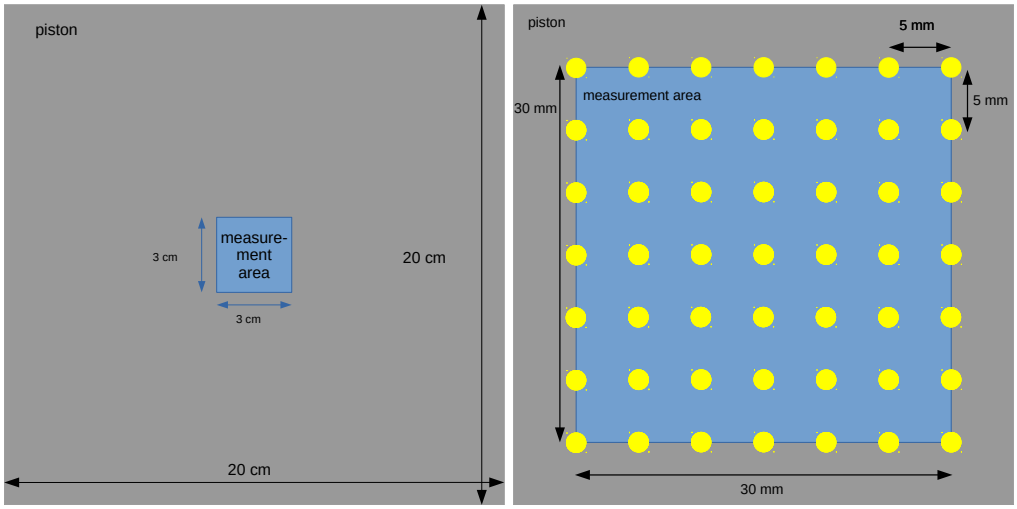

(a) original (b) zoomed setup

Figure 5.1: Measurement setup: grey area = piston area, blue area = measurement area, yellow dots = measurement positions.

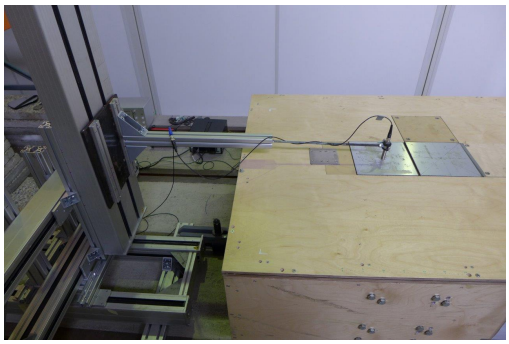

(a) overview

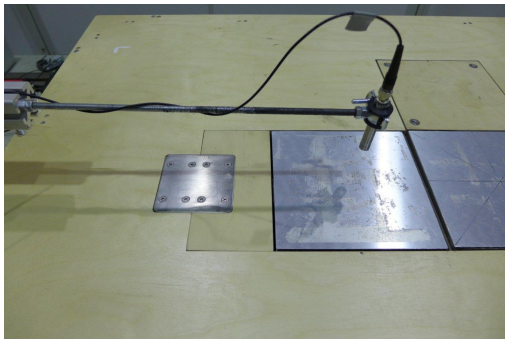

(b) microphone

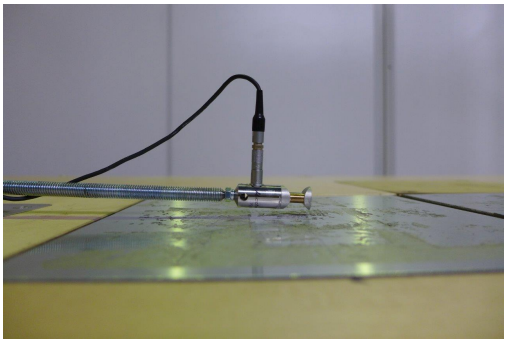

(c) PU probe

Figure 5.2: Details of the measurement setup.

The velocity probe's polar pattern (directionality) has a cos(θ) characteristic or a figure of eight response (see figure 5.3). So if an angular positioning error of e.g. 10° degrees occurs, the absolute error equals 20log(cos(10°)) = 0.133 dB. This directivity is applied if the probe is rotated around the axis, where it is mounted (see figure 5.2 c). In this picture one can also clearly see an inclination error of the velocity sensor positioning. Unfortunately, there is no knowledge about the errors produced with this inclination, but it is expected that the probe is not very sensitive to these errors and therefore it does not play an important role. Furthermore, the packaging with the two cylinders rises the particle velocity level. This increase is mainly caused by a channelling effect: the particle flow is forced through the package causing a level increase [5].

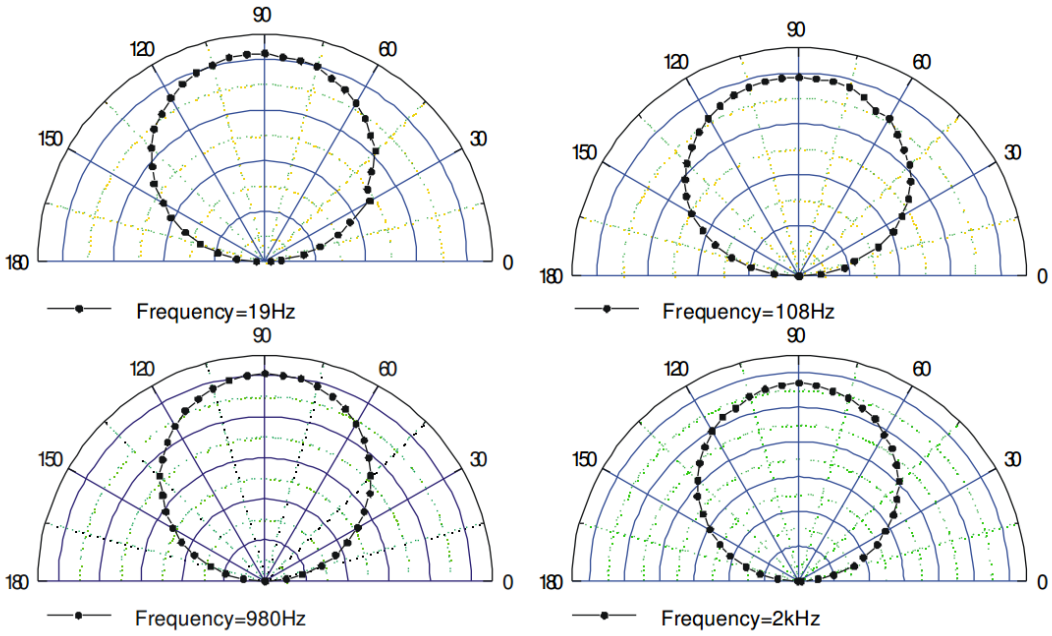

Figure 5.3: Polar patterns of a velocity probe at different frequencies (linear scale, only half the response is measured) [5].

Calibration

The G.R.A.S. microphone is calibrated with a Brüel and Kjær calibrator. For the calibration of the acceleration sensor the data from the manufacturer's calibration sheet is used. A separate dayle calibration of the sensor would be much effort, because of it being installed inside the box. The manufacturer gives a value of 1.008$\frac{pC}{m/s^2}$.

Relevant Frequency

The Tbox is used for material characterization up to around 1000 Hz. Up to this frequency the coherence function is almost unity and the FRF is flat (see figures 5.4 - 5.7). Above 1000 Hz resonances of the piston appear (e.g. at 1500 Hz in figure 5.6) and the coherence function collapses (figure 5.4), because the measured acceleration converges to zero or has an abrupt minimum.

If only use the center points are used for the analysis and calibration, it would be possible to take specific frequencies where the coherence has a high value (e.g. at 1700, 2500, 3100, 4000, 4800 and 5300 Hz; see figure 5.4). But if it is required to use positions up to $\pm$ 10 mm away from the central position, it is hard to find frequencies especially above 5000 Hz, where the coherence is good for all measurement points (see figure 5.5). Therefore, frequencies from 50 Hz to 1000 Hz are used for the main evaluation in this section, because in this frequency range, the piston does not have any resonance and the coherence function is unity (see figure 5.7). The methodology can be expanded to higher frequencies. Provided that frequencies, where no modes occur and the coherence function is high, are selected. If a smaller piston is used, the modes are shifted to a higher frequency range.

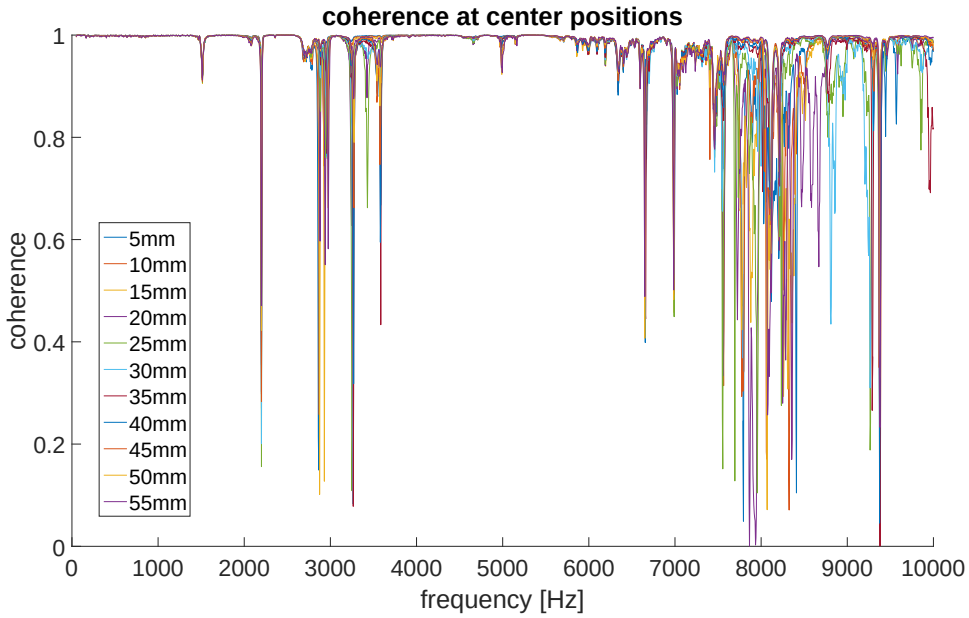

Figure 5.4: Coherence in different layers at center positions.

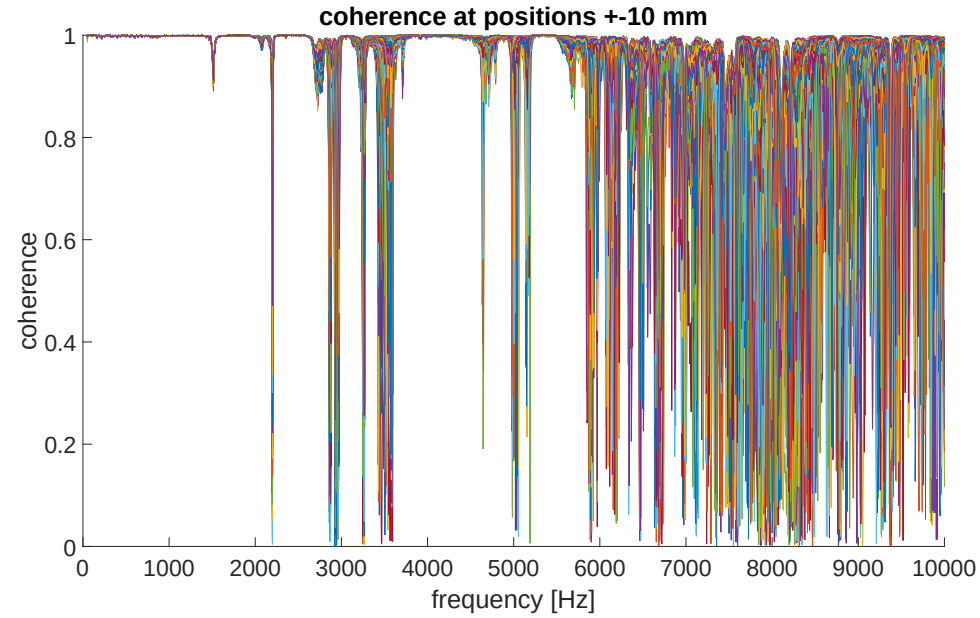

Figure 5.5: Coherence in different layers at positions up to ± 10 mm in x- and/or y-direction.

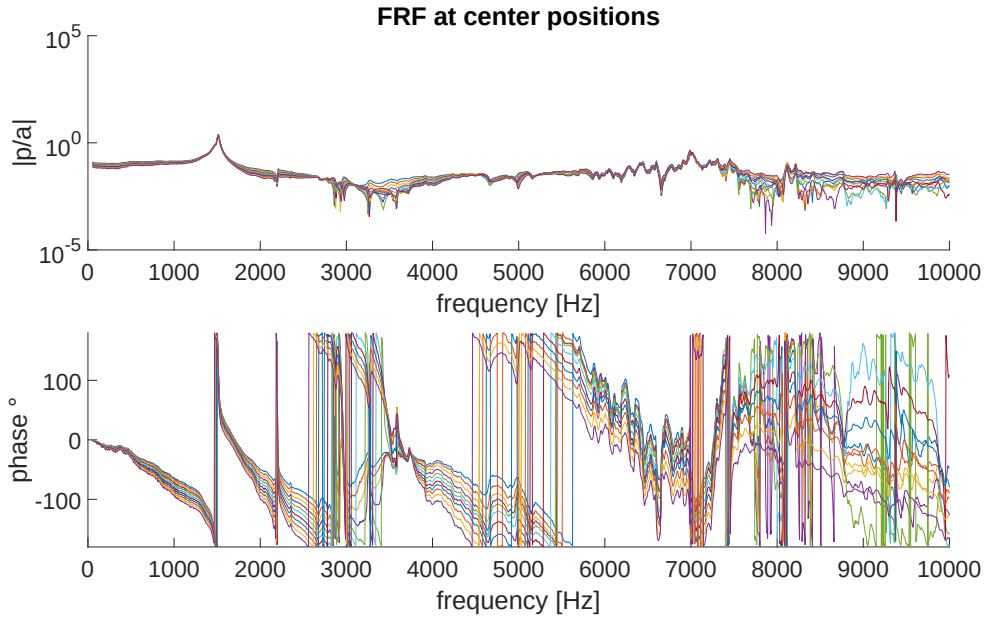

Figure 5.6: Absolute value and phase of the FRF at center center positions: 50 Hz - 10kHz.

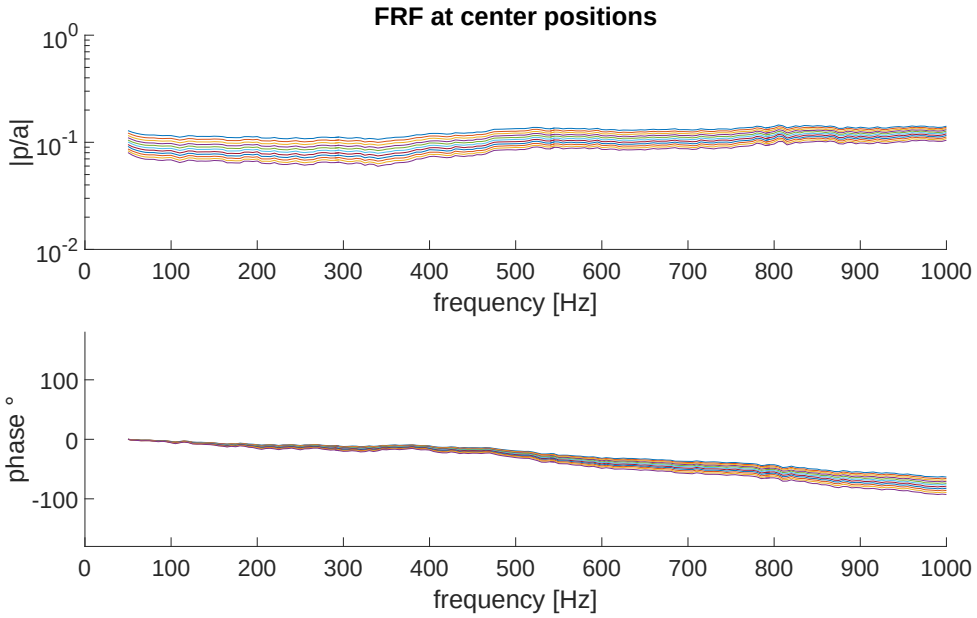

Figure 5.7: Absolute value and phase of the FRF at center center positions: 50 Hz to 1000 Hz.

5.2 Using Different Distances for FD Calculation

The first analysis focuses on the obtained velocity in z-direction at specific points using FD with different spacing. Column 1 of figure 5.8 shows the obtained absolute velocity with FD v_{FD} relative to the surface velocity of the piston v_P for the center positions computed at layers 20 mm and 40 mm above the piston using a spacing of 10, 20 and 30 mm for the FD calculations. One can see that the obtained values are subject to fluctuations.

On the one hand, these can occur from the subtraction of two almost equal values. It seems that there are not enough digits to be precise enough, which leads to round off errors. These errors are random and can be removed by using frequency-band averaged values.

On the other hand, if two almost equal quantities are subtracted, the noise in the measurements disturbs this subtraction, because the noise is random and therefore is different in every measurement. High coherence is needed. Bendat and Piersol [36] provide formulas with which the random error in the amplitudes of the measured FRFs can be estimated and confidence intervals can be calculated with the help of the coherence value γ^2 and the number of averages n_d.

The random error ϵ in the amplitudes and an approximate confidence interval of 95% are estimated as follows:

$$\epsilon(|\mathrm{FRF}|) = \frac{(1-\gamma^2)^{\frac{1}{2}}}{|\gamma^2|\sqrt{2n_d}} \tag{5.1}$$

$$[|\mathrm{FRF}| \cdot (1-2\epsilon) \leq |\mathrm{FRF}| \leq |\mathrm{FRF}|(1+2\epsilon)] \tag{5.2}$$

The coherence function in 5.4 shows that the value is never smaller than 0.99 over the frequency range of 50 Hz to 1000 Hz. As mentioned in the measurement setup section, the number of averages was set to 100. The following random error and confidence interval of 95% are obtained:

$$\epsilon(|\mathrm{FRF}|) = \frac{(1-\gamma^2)^{\frac{1}{2}}}{|\gamma^2|\sqrt{2n_d}} = \frac{\sqrt{(1-0.99)}}{\sqrt{0.99 \cdot 2 \cdot 100}} = 0.0071 \tag{5.3}$$

$$[|\mathrm{FRF}| \cdot 0.986 \leq |\mathrm{FRF}| \leq |\mathrm{FRF}| \cdot 1.014] \tag{5.4}$$

From these calculations it follows that the obtained absolute value lies within a confidence interval of $\pm$ 1.4 % with a probability of 95 %.

If the FRF functions shall have a maximum error of 1 dB with a probability of 95 %, the needed coherence value can be calculated using equations 5.1 and 5.2:

$$\mathrm{FRF}_{\mathrm{error,max}} = -1\,\mathrm{dB} \tag{5.5}$$

$$(1-2\epsilon) = 10^{\frac{-1}{20}} = 0.8913 \tag{5.6}$$

$$\epsilon = 0.0544 \tag{5.7}$$

$$\gamma^2 = \frac{1}{\epsilon^2 \cdot 2 \cdot n_d + 1} = \frac{1}{0.0059 \cdot n_d + 1} \tag{5.8}$$

For n_d = 100, a coherence value γ^2 of 0.63 is obtained. A maximum error of 0.5 dB using n_d = 100 leads to a value of γ^2 = 0.87 and a maximum error of 0.25 dB using n_d = 100 to γ^2 = 0.96.

As a next step the maximum error of the velocity calculation is calculated

$$\begin{aligned}\left(\frac{v+\Delta}{v}\right)_{\max} &= \frac{\frac{p_2(1+2\epsilon)-p_1(1-2\epsilon)}{d}\frac{1}{i\rho\omega}}{\frac{p_2-p_1}{d}\frac{1}{i\rho\omega}} = \frac{p_2(1+2\epsilon)-p_1(1-2\epsilon)}{p_2-p_1} \\ &= \frac{p_2-p_1+2(p_2+p_1)\epsilon}{p_2-p_1} = 1+2\epsilon\frac{p_2+p_1}{p_2-p_1} \\ &= 1+2\epsilon\frac{\frac{p_2}{p_1}+1}{\frac{p_2}{p_1}-1},\end{aligned} \tag{5.9}$$

where d is the physical measurement distance between p_1 and p_2.

The maximum velocity error depends on the random error ϵ as well as on the amplitudes of p_1 and p_2. In the beginning, the piston will act a bit more like a plane wave, where the amplitudes of p_1 and p_2 are equal. As a worst case scenario a monopole with spherical propagation is assumed. The amplitude ratio $|\frac{p_2}{p_1}|$ equals $\frac{r+d}{r} = 1+\frac{d}{r}$, where d is the measurement distance between p_1 and p_2 and r the spacial distance between the source and p_2.

By using equation 5.9 it follows that:

$$\left(\frac{v+\Delta}{v}\right)_{\max} = 1+2\epsilon\frac{2+\frac{d}{r}}{\frac{d}{r}} = 1+2\epsilon = 1+2\epsilon\left(\frac{2r}{d}+1\right) \tag{5.10}$$

Consequently, the maximum velocity error depends on ϵ, the measurement distances and the used FD distance.

FD calculations with 10 mm distance (FD10) have the most fluctuations and FD calculation with 30 mm (FD30) the least. Therefore, the complex velocity values are smoothed by using a moving average (ma). A moving average of 5 (ma5) uses the actual frequency value and 2 frequency values before and 2 afterwards. From these 5 values the mean is computed and used as result. Consequently, ma = 19 (ma19) computes the mean from 19 frequency pins ($\pm$ 45 Hz).

Figure 5.8 also shows that the value at a distance of 20 mm obtained with FD30 is higher compared to the values obtained with FD10 and FD20. This may be due to the fact that FD30 uses the pressure layers at 5 mm and 35 mm for the calculations and at 5 mm interference effects can appear and amplify the pressure. Furthermore, this could also be caused by the near field, for which more layers may be needed to improve the results.

When ma = 19 at a distance of 40 mm is used, all FD curves are overlapping. At a distance of 20 mm the FD10 curve approaches the FD20 curve because the measurement layers used are already out of the near field.

A problem of moving average is that one must take care that only random fluctuations due to noise and round off errors are eliminated and fluctuations which occur due to the system are kept.

If ma = 19 (Δf = 90 Hz) is used, the small fluctuations are removed properly but large fluctuations (e.g. the rise of the curve at approx. 530 Hz) can still be seen clearly. Therefore, ma = 19 is used for all further investigations in this thesis.

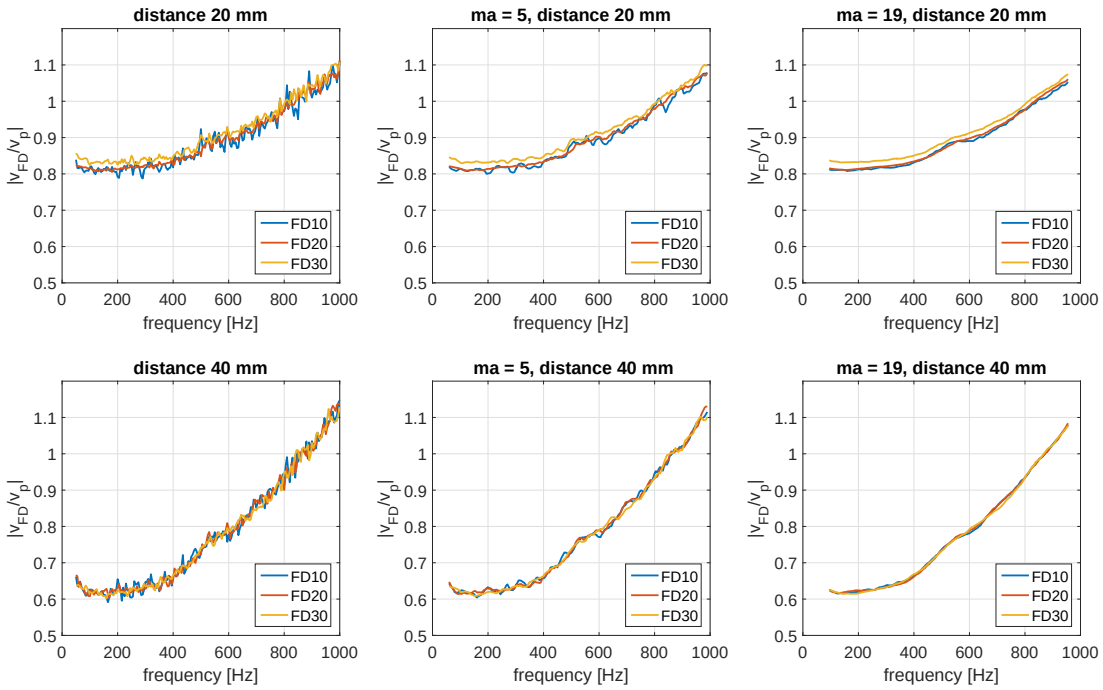

Figure 5.8: $|v_{FD}/v_P|$ Amplitude of the particle velocity in z-direction relative to the surface velocity at center positions for difference FD calculations at a distance of 20 mm above the piston (row 1), a distance of 40 mm above the piston (row 2), without smoothing (column 1), smoothing moving average of 5 (column 2) and smoothing moving average of 19 (column 3).

5.3 Finding the best Position for Calibration

The last section showed that the use of smoothing is recommended before working on the next steps. Furthermore, using a larger spacing also reduces the

fluctuations. Therefore, the results obtained with FD20 are used in this section because the finite differences are also computed in x- and y-direction to check for lateral velocities and a stable sound field. If FD30 would be used, only one velocity value per layer could be computed due to the maximum distance of the measurement points of 30 mm (see figure 5.1) and therefore no comparison between different layer positions would be possible.

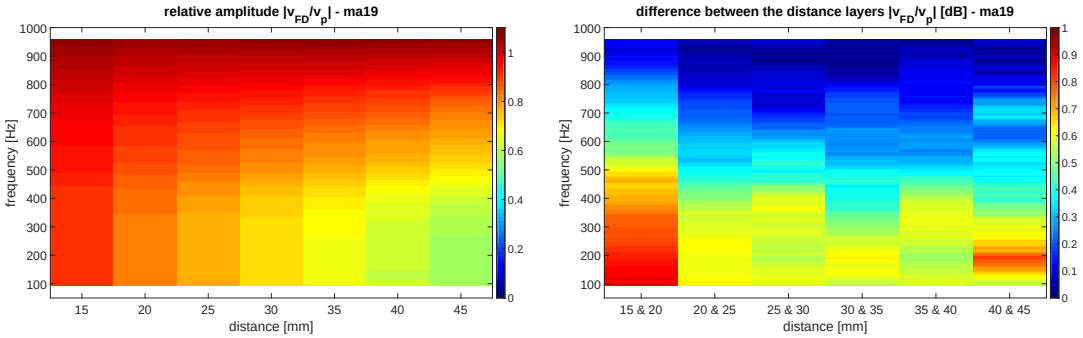

Figure 5.9: Left: $|v_{FD}/v_P|$ amplitude of the particle velocity in z-direction relative to the surface velocity at center positions using ma19, right: difference between the distance layer values in dB using ma19.

In order to find the best calibration position the sound field above the piston is analyzed. In the next pages only the velocity vector in z-direction (normal to the piston) is used. Metzger and Kaltenbacher [13] simulated the behavior of the sound field and showed some interesting plots. Some of their analyses are conducted with our real measurement data.

The amplitudes of the particle velocity in z-direction relative to the surface velocity at center positions using different ma factors are plotted at the left side of figure 5.9 and the level difference in of these amplitudes in dB is plotted on the right side of figure 5.9. It can be seen, that a ma factor of 19, leads to smooth transitions. Because of the large piston size, interference can occur and lead to relative amplitude values slightly bigger than a level of one for high frequencies. Furthermore, the difference between the layers is smaller for high frequencies and for distances further away from the piston.

During the calibration process, location errors can occur because one must position the velocity sensor exactly in the middle between the two microphone positions. Therefore, as a first indicator for positioning, the sum of the level differences in dB is calculated

$$\frac{1}{N}\sum_{k=1}^{N}\left|\frac{\partial}{\partial z}\left|\frac{v_{FD}}{v_P}(f_k)\right|\right|, \tag{5.11}$$

where N is the number of evaluated frequencies and plotted on the right site of figure 5.10. A small value indicates little change between the layers and therefore less positioning error. From this point of view a calibration at a distance of 25 - 35 seems to fit best.

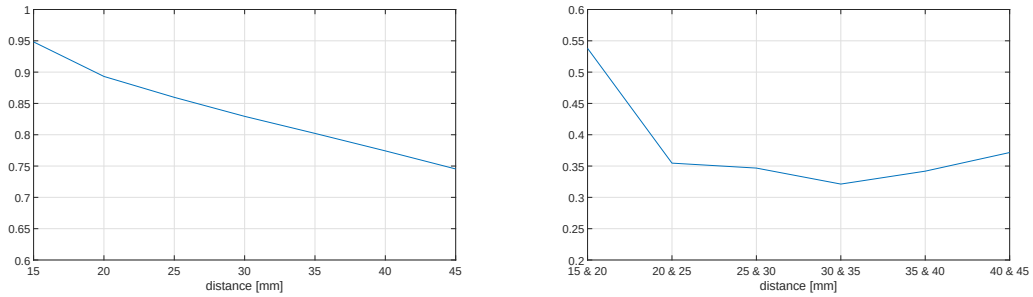

Figure 5.10: Left: $|v_{FD}/v_P|$ amplitude of the particle velocity in z-direction relative to the surface velocity at center positions using different ma factors, right: difference between the distance layer values in dB.

Moreover, Metzger and Kaltenbacher [13] pointed out that a higher particle velocity amplitude leads to better SNRs. Thus, as a second step, the summation over the amplitudes is performed

$$\frac{1}{N}\sum_{k=1}^{N}\left|\frac{v_{FD}}{v_P}(f_k)\right|, \tag{5.12}$$

and plotted on the left site of figure 5.10. The summation value decreases with increasing distance, but due to the large size of the plate the decreasing process is quite slow and still has a reasonable value at 25 or 35 mm.

In a third step, the difference between the obtained velocity values within a layer (differences in x- and y-direction) are calculated. The aim of these calculations is to find out how precise one has to be in x- and y-direction. Therefore, all obtained absolute velocity results in a layer are compared to the absolute value at the center positions. The other velocity values lie in a square around the center position with the size of $\pm$ 5 mm. When using a ma of 19, already no differences greater 0.2 dB are obtained in all layers. This shows that in all the

layers used, a positioning, within a 5x5-mm-square around the center position without having an error bigger than 0.4 dB, is possible.

As a fourth analysis, absolute values of positions in a 5x5-mm-square layer (x- and y-direction), which are $\pm$ 5 mm away from the layer in z-direction used as a reference, are compared to the absolute value at the center position of the reference layer. With the use of ma19, errors larger than 0.8 dB only occur if the layers with 20 and 40 mm distance are used as reference layers. When using layers with 25 - 35 mm distance no errors greater than 0.8 dB are obtained.

Finally, also the error due to the estimation of the FRF is included using equation 5.10 and $d = r = 0.02$ for FD20 and a calculation distance of 30 mm.:

$$\left(\frac{v+\Delta}{v}\right)_{\max} = 1 + 2\epsilon\left(\frac{2 \cdot 0.002}{0.002} + 1\right) = 1 + 2\epsilon(2+1) = 1 + 6\epsilon \tag{5.13}$$

Assuming a maximum error of the velocity in dB $v_{\text{error,max,dB}}$, ϵ can be calculated with the following equation:

$$\epsilon = \frac{10^{\frac{v_{\text{error,max,dB}}}{20}} - 1}{6} \tag{5.14}$$

The result is then inserted in equation 5.8 to get a minimum coherence value. Results for different maximum velocity errors in dB are shown in table 5.1.

$v_{\text{error,max}}$ [dB]	ϵ	γ^2
0.2	0.0039	0.997
0.25	0.0049	0.995
0.3	0.0059	0.993
0.35	0.0069	0.991

Table 5.1: Values for the random error ϵ and the coherence γ^2 for different maximum velocity errors in dB.

The coherence functions for all obtained pressure measurements over a frequency range of 50 to 1000 Hz show a coherence higher than 0.991. Subsequently, an error of 0.35 dB must be added to the value of 0.8 dB.

Accordingly, when the calibration is performed in one of the three layers between 25 and 35 mm above the piston, it is possible to position the probe within a 5x5x5-mm-cube around the center position, without having an error bigger than 1.15 dB.

Up to this point, only the amplitudes of the velocity vector in z-direction are analyzed. Therefore, in the fifth step the FD is calculated in x- and y-direction as well and the absolute value of the obtained velocity value is compared to a vector pointing only in z-direction. The angle between these two vectors gives information, if the measured velocity is mainly pointing in z-direction (as assumed) or if there are lateral velocities as well (e.g. due to reflections in the measurement environment). It can be seen that for most of the frequencies at all positions the angle between the z-axis and the calculated velocity vector is smaller than 10°. This results from the fact that the velocity vectors in x- and y-direction are only up to 15 % of the size of the velocity vector in z-direction. Ideally the vectors in x- and y-direction should be zero.

However, for frequencies between 565 and 625 Hz the velocity vector in x-direction has about 60 % of the length of the velocity vector in z-direction. A way to explain this value could be a reflection due to the z-axis of the positioning system. The axis is 25.5 cm wide and extends 70 cm beyond the Tbox. This leads to a problem in case both pressure and velocity transducers should be calibrated. Then, the velocity probe measures a wrong resulting vector. The vectors in x- and z-direction lead to an amplitude of the resulting vector which is longer/higher than the amplitude of a vector only having a main component in z-direction. However, the polar pattern of the velocity sensor has a figure of eight response (cosinusoidal directionality) and therefore dampens the amplitude of vectors which are not exactly coming from z-direction. The error is thus eliminated. In principle the velocity probe is insensitive to lateral fields. So on the one hand the velocity sensor is insensitive to lateral field, having a cross sensitivity of 0.05. The value of 5 % was previously determined at VIRTUAL VEHICLE with experiments. But on the other hand, if the pressure sensor needs to be calibrated as well, the lateral field is of importance, because the pressure sensor has no directivity.

The resulting velocity vectors at 595 Hz and at a distance of 30 mm are plotted in figures 5.11 and 5.12 . At 595 Hz the vectors point to the direction of the x- and the z-axis and in comparison at 500 Hz the vector in z-direction is dominant.

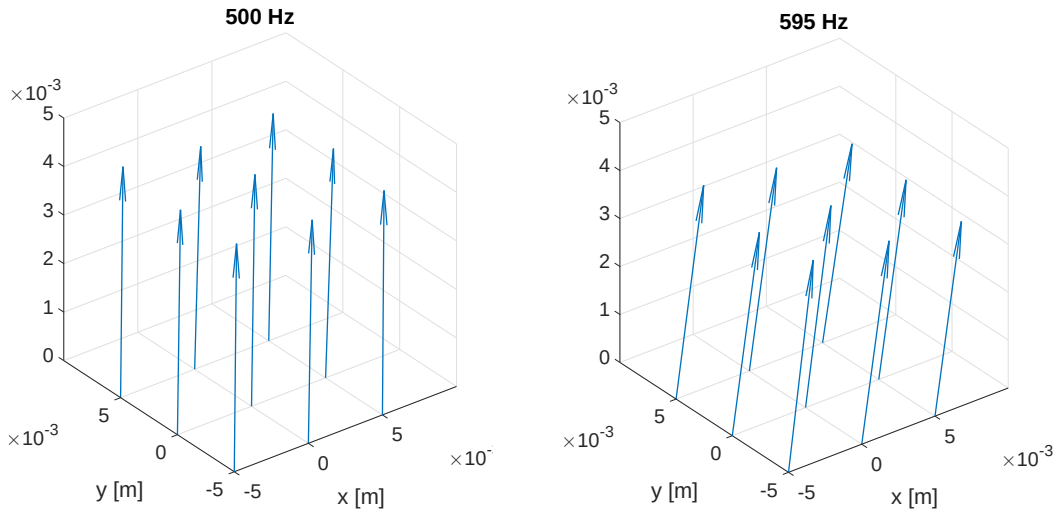

Figure 5.11: Elevation plots of the velocity vectors at a distance of 30 mm for 500 and 595 Hz with automatically scaled length to fit within the grids.

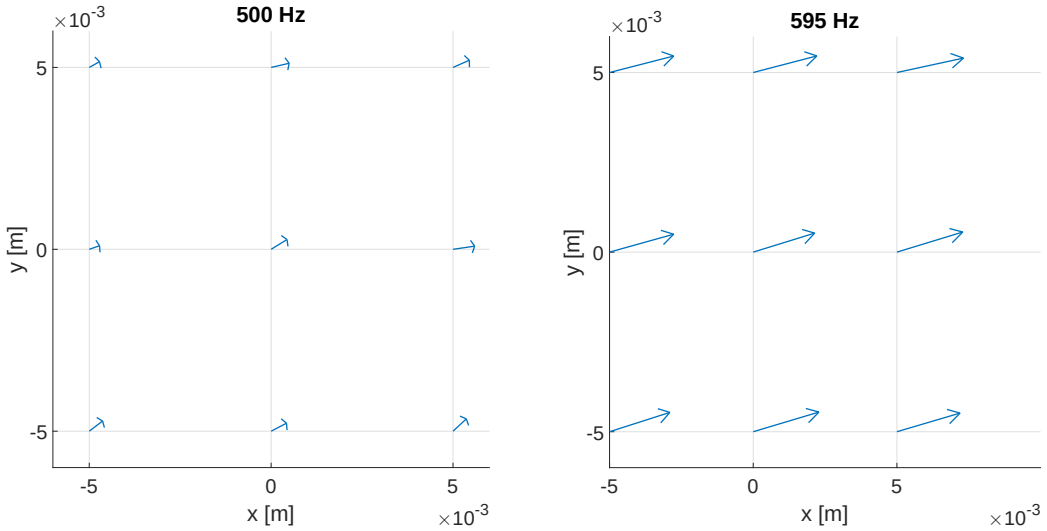

Figure 5.12: Outline plots of the velocity vectors at a distance of 30 mm for 500 and 595 Hz with automatically scaled length to fit within the grids.

5.4 Calibration Curves

in order to obtain a calibration curve, the voltage output obtained with the PU probe at a certain location is divided by the velocity in z-direction calculated with FD (from the measured pressure data) in the same location.

In figures 5.14 and 5.13 the calibration results obtained with the measurement data using the distance layer at 30 mm are shown. The red lines display the results with the calibration method presented in this work. Moreover, the blue line represents the sensitivity model given by the manufacturer Microflown. For the results in figure 5.14 only the calculated FD velocity at the center position is used (x = 0, y = 0, z = 30). In rows 1 and 2 of figure 5.13 the calculated velocity is a mean value of all 9 obtained values at the 30 mm layer and in rows 3 and 4 of figure 5.13 the mean of 27 obtained values (layers 25, 30 and 35 mm) is used as calculated velocity.

It should be pointed out that the obtained sensitivities differ from the ones given by Microflown. The real values between 95 and 150 Hz and 475 and 1000 Hz obtained with the red calibration are lower compared to the blue correction curve of Microflown. For frequencies between 150 and 475 Hz the values are larger. The imaginary values are smaller than the ones from the sensitivity model, with an exception from 120 to 220 Hz, where the values match.

As mentioned in the last section, there is a reflection in x-direction between 565 and 625 Hz, which can also be seen in the calibration curves (especially in the absolute value plot). The reflection influences the measured velocity as well. In order to get a clean calibration curve the obtained values must be corrected with a curve which refits the values between 565 and 625 Hz using the values before 525 Hz and after 625 Hz and uses a logical continuation. Another method would be correcting the measured velocity curve beforehand or correct the calculated measurement curve by using the calculated length of the vector instead of using the absolute value of the velocity vector in z-direction only.

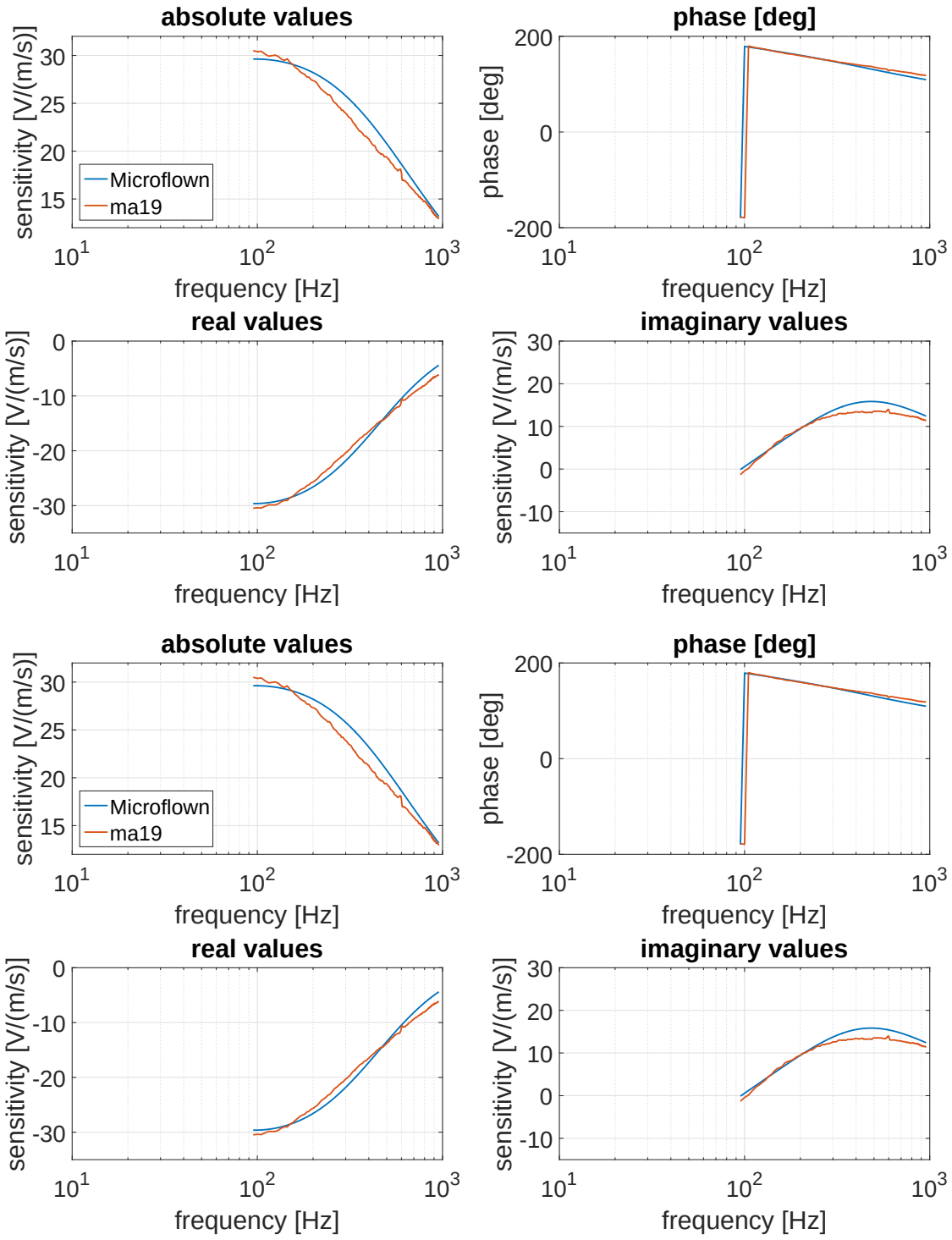

Figure 5.13: Calibration curve obtained at a distance of 30 mm using the mean values of all 9 obtained positions of the calculated velocity in this layer (top) / the mean values of 27 obtained positions of the calculated velocity in layers 25 - 35 mm (bottom) compared to the curve given by Microflown.

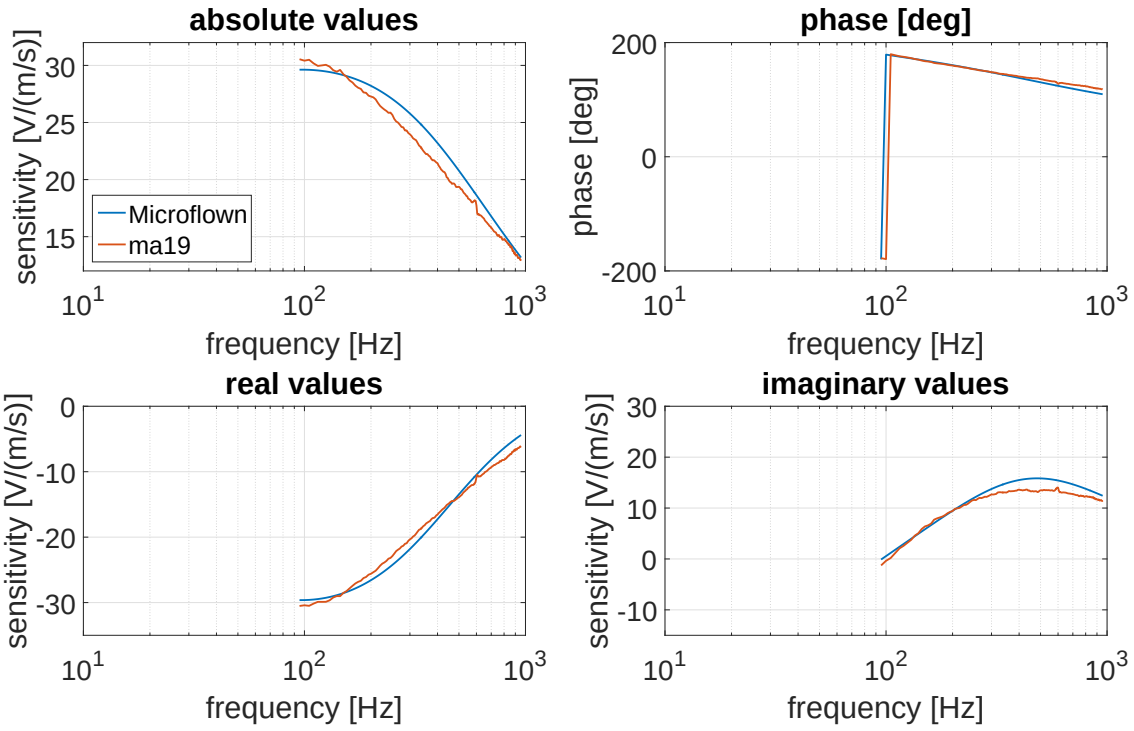

Figure 5.14: Calibration curve obtained at a distance of 30 mm using the center position of the calculated velocity compared to the curve given by Microflown.

5.5 Summary of the Finite Difference Experiments

The results obtained with the FD experiments show that it is possible to calibrate a particle velocity probe with a piston in an appropriate manner. The calibration is done at positions above the center of the piston because there the velocity field turned out to be stable and the main component of the 3D velocity vector is pointing into z-direction. The calibration in this thesis is executed over a frequency range from 50 Hz to 1000 Hz, because the Tbox measurements are also performed only up to 1000 Hz. For higher frequencies the structural modal properties of the piston have significant influence on the measurement and calculation results and thereby on the stability of the field and the calculated sensitivity. In order to obtain a reasonable calibration curve on top of the effective applicable frequency range of the Tbox, the frequencies used above 1000 Hz would have to be picked carefully at frequency positions where no resonances and antiresonances appear in the FRFs and where the coherence

function is close to unity (e.g. at 1700, 2500, 3100, 4000, 4800 and 5300 Hz; see figure 5.4).

For a verification of the procedure the calibration and field analysis should be done with pistons of different sizes as well, because for smaller pistons the frequencies where modes occur are shifted to higher frequencies and the field analysis and calibration could be done e.g. up to 5000 Hz without the need of picking specific frequencies in the higher frequency area.

The following steps have to be performed for the calibration procedure with a total precision of 1.15 dB presented in this thesis:

- Choose a calibration distance of 30 mm.
- To avoid an error larger than 0.35 dB due to the estimation of the FRF: Use 100 averages and control that the coherence value is bigger than 0.991 over the whole frequency range used for calibration.
- Smooth the curves with a moving average factor, which reduces the round off errors (e.g. ma19).
- Analyze the velocity field above the piston: Verification that the changes of the absolute velocity vectors in z-direction inside a measurement cube are smaller than 0.8 dB. Therefore, calculate the velocity at the center position (x = y = 0, z = 30 mm), where the velocity sensor is calibrated and at the edge positions of the cube. 18 pressure positions are needed. The measurement positions are shown in table 5.2 for FD20.

$v(x[mm], y[mm], z[mm]$	$p_1(x[mm], y[mm], z[mm]$	$p_2(x[mm], y[mm], z[mm]$
$v_{\text{ref}}(0,0,30)$	$p_{\text{ref},1}(0,0,40)$	$p_{\text{ref},2}(0,0,20)$
$v_{\text{edge1}}(5,5,25)$	$p_{\text{edge1},1}(5,5,35)$	$p_{\text{edge1},1}(5,5,15)$
$v_{\text{edge2}}(-5,5,25)$	$p_{\text{edge2},1}(-5,5,35)$	$p_{\text{edge2},2}(-5,5,15)$
$v_{\text{edge3}}(-5,-5,25)$	$p_{\text{edge3},1}(-5,-5,35)$	$p_{\text{edge3},2}(-5,-5,15)$
$v_{\text{edge4}}(5,-5,25)$	$p_{\text{edge4},1}(5,-5,35)$	$p_{\text{edge4},2}(5,-5,15)$
$v_{\text{edge5}}(5,5,35)$	$p_{\text{edge5},1}(5,5,45)$	$p_{\text{edge5},1}(5,5,25)$
$v_{\text{edge6}}(-5,5,35)$	$p_{\text{edge6},1}(-5,5,45)$	$p_{\text{edge6},2}(-5,5,25)$
$v_{\text{edge7}}(-5,-5,35)$	$p_{\text{edge7},1}(-5,-5,45)$	$p_{\text{edge7},2}(-5,-5,25)$
$v_{\text{edge8}}(5,-5,35)$	$p_{\text{edge8},1}(5,-5,45)$	$p_{\text{edge8},2}(5,-5,25)$

Table 5.2: Measurement and calculation positions needed for the calibration procedure with FD20; column 1: positions, where velocity is calculated, columns 2 and 3: positions, where the pressure must be measured to calculated the velocity in column 1.

6 Conclusion and Outlook

This thesis started with a brief introduction on PU probes and motivates the need for a development of a calibration procedure for the acoustic particle velocity sensor. A vibrating piston has been chosen as exciter and different methodologies to obtain a reference velocity are presented in chapter 2.

The accuracy of the obtained reference velocities are the matter of the research conducted in chapters 3 and 4. In chapter 3 it was shown that Near Field Acoustical Holography (NAH) is suitable for the characterization of a field, but if the measurement area is too small, no reliable velocity values can be calculated. When using a larger measurement area, as shown in chapter 4, the velocity values computed with NAH have a high accuracy and therefore could be used for calibration. The calculations using Statistically Optimized Near Field Acoustical Holography (SONAH) in chapters 3 and 4 showed that further research concerning the correct use of the scaling functions and a proper implementation of the integrals would be needed to get reliable results for calibration.

The results obtained in chapters 3 and 4 with the Finite Difference method (FD) seem to be promising. Since the complexity of FD in terms of measurement efforts and calculation time is by far smaller compared to NAH, FD has be chosen for the investigations in chapter 5. The calibration method using the FD scheme is promising. A validation of the simulations and theoretical assumptions is performed with measurements conducted at VIRTUAL VEHICLE. Analysis of these measurements show that it is possible to calibrate a velocity probe in an appropriate manner. A positioning error within a cube with the size of 1x1x1 cm of 0.8 dB maximum and a maximum overall error of 1.15 dB is obtained.

The following tasks have to be evaluated in further research:

- Identification of stable calibration points above 1000 Hz using the piston of the trim test rig (Tbox).
- Extension of the presented calibration curve to higher frequencies.
- Verification of the calibration procedure with different pistons (e.g. using a piston with smaller dimensions).
- Determination of the most appropriate moving average (ma) factor.
- Influence of the inclination error due to the positioning.

Bibliography

[1] Christopher G. Albert, Giorgio Veronesi, Eugène Nijman, and Jan Rejlek. Prediction of the vibro-acoustic response of a structure-liner-fluid system based on a patch transfer function approach and direct experimental subsystem characterisation. *Applied Acoustics*, 112:14–24, 2016.

[2] Morvan Ouisse, Laurent Maxit, Christian Cacciolati, and Jean-Louis Guyader. Patch transfer functions as a tool to couple linear acoustic problems. *Journal of vibration and acoustics*, 127(5):458–466, 2005.

[3] Mathieu Aucejo, Laurent Maxit, Nicolas Totaro, and J-L Guyader. Convergence acceleration using the residual shape technique when solving structure–acoustic coupling with the patch transfer functions method. *Computers & Structures*, 88(11-12):728–736, 2010.

[4] Goran Pavić. Air-borne sound source characterization by patch impedance coupling approach. *Journal of Sound and Vibration*, 329(23):4907–4921, 2010.

[5] Hans-Elias de Bree. The microflown e-book, 2009. Online; accessed March 2018; www.microflown.com/library/books/the-microflown-e-book.htm.

[6] Finn Jacobsen and Hans-Elias de Bree. Measurement of sound intensity: p-u probes versus p-p probes. In *Proceedings of Noise and Vibration Emerging Methods*, 2005.

[7] Finn Jacobsen and Virginie Jaud. A note on the calibration of pressure-velocity sound intensity probes. *The Journal of the Acoustical Society of America*, 120(2):830–837, 2006.

[8] Tom GH Basten and Hans-Elias de Bree. Full bandwidth calibration procedure for acoustic probes containing a pressure and particle velocity sensor. *The Journal of the Acoustical Society of America*, 127(1):264–270, 2010.

[9] Virginie Jaud and Finn Jacobsen. Calibration of pu intensity probes. In *6th European Conference on Noise Control*, 2006.

[10] Stefan Kaiser and Mathias Wutti. Kalibrierung von pv-sonden. Bachelor's thesis, Graz University of Technology, Signal Processing and Speech Communication Laboratory, 2013.

[11] Daniel Fernandez Comesaña, Triantafillos Koukoulas, Ben Piper, and Erik-Jan Jongh. Calibration of acoustic particle velocity sensors using a laser based method. In *23rd International Congress on Sound and Vibration*, pages 1–8, 2016.

[12] Wen-Qian Jing, Yong-Bin Zhang, and Chuan-Xing Bi. A nearfield acoustic holography-based method for measuring the sensitivity of a particle velocity sensor. *Acta Acustica united with Acustica*, 101(4):855–858, 2015.

[13] Jochen Metzger and Manfred Kaltenbacher. Simultaneous calibration method for a 3d particle velocity sensor. *Acta Acustica united with Acustica*, 103(2):252–261, 2017.

[14] Earl George Williams. *Fourier Acoustics: Sound Radiation and Nearfield Acoustical Holography*. Academic Press, 1999.

[15] Earl G Williams. Use of near-field acoustical holography in noise and vibration measurements. In Malcolm J. Crocker, editor, *Handbook of Noise and Vibration Control*, chapter 50, pages 598–611. Wiley Online Library, 2008.

[16] Daniel Hofer. Implementierung eines 64 kanal mikrofonarrays. Master's thesis, University of Music and Performing Arts Graz, Institute of Electronic Music and Acoustics, 2008.

[17] Earl G Williams. Regularization methods for near-field acoustical holography. *The Journal of the Acoustical Society of America*, 110(4):1976–1988, 2001.

[18] Seong-Ho Yoon and Philip A Nelson. Estimation of acoustic source strength by inverse methods: Part ii, experimental investigation of methods for choosing regularization parameters. *Journal of sound and vibration*, 233(4):665–701, 2000.

[19] Per Christian Hansen. *Rank-deficient and discrete ill-posed problems: numerical aspects of linear inversion*. SIAM, 1998.

[20] Gene H Golub, Michael Heath, and Grace Wahba. Generalized cross-validation as a method for choosing a good ridge parameter. *Technometrics*, 21(2):215–223, 1979.

[21] Jørgen Hald. Beamforming and wavenumber processing. In *Handbook of Signal Processing in Acoustics*, pages 131–144. Springer, 2008.

[22] Rick Scholte. *Fourier based high-resolution near-field sound imaging*. PhD thesis, Eindhoven University of Technology Department of Mechanical Engineering, 2008.

[23] Nicolas P Valdivia and Earl G Williams. Study of the comparison of the methods of equivalent sources and boundary element methods for near-field acoustic holography. *The Journal of the Acoustical Society of America*, 120(6):3694–3705, 2006.

[24] Julian D Maynard, Earl G Williams, and Y Lee. Nearfield acoustic holography: I. theory of generalized holography and the development of nah. *The Journal of the Acoustical Society of America*, 78(4):1395–1413, 1985.

[25] Finn Jacobsen and Yang Liu. Near field acoustic holography with particle velocity transducers. *The Journal of the Acoustical Society of America*, 118(5):3139–3144, 2005.

[26] Jørgen Hald. Basic theory and properties of statistically optimized near-field acoustical holography. *The Journal of the Acoustical Society of America*, 125(4):2105–2120, 2009.

[27] Jørgen Hald. Scaling of plane-wave functions in statistically optimized near-field acoustic holography. *The Journal of the Acoustical Society of America*, 136(5):2687–2696, 2014.

[28] Theodore J Schultz. Acoustic wattmeter. *The Journal of the Acoustical Society of America*, 28(4):693–699, 1956.

[29] Werner Weselak. *Akustische Messtechnik Skript zur gleichnamigen Vorlesung*. Technische Universität Graz, version 9.0 edition, 2014.

[30] Michael Möser. *Messtechnik der Akustik*. Springer-Verlag, 2009.

[31] Brüel and Kjær. *Sound Intensity*. www.bksv.com/media/doc/bro476.pdf, 1993.

[32] Finn Jacobsen, Vicente Cutanda, and Peter M Juhl. A numerical and experimental investigation of the performance of sound intensity probes at high frequencies. *The Journal of the Acoustical Society of America*, 103(2):953–961, 1998.

[33] Earl G Williams, Brian H Houston, and Peter C Herdic. Fast fourier transform and singular value decomposition formulations for patch nearfield acoustical holography. *The Journal of the Acoustical Society of America*, 114(3):1322–1333, 2003.

[34] Yong-Bin Zhang, Finn Jacobsen, Chuan-Xing Bi, and Xin-Zhao Chen. Patch near field acoustic holography based on particle velocity measurements. *The Journal of the Acoustical Society of America*, 126(2):721–727, 2009.

[35] Philipp Schmidt. Improvements in localization of planar acoustic holography. Master's thesis, Universtiy of Music and Performing Arts Graz, Institute of Electronic Music and Acoustics, 2012.

[36] Julius S Bendat and Allan G Piersol. *Random data: analysis and measurement procedures*, volume 729. John Wiley & Sons, 2011.

List of Figures

List of Abbreviations

DFT	discrete Fourier transform
FD	finite difference
FRF	frequency response function
GCV	generalized cross validation
ma	moving average
NAH	Near Field Acoustical Holography
PM	phase mismatch
PP probe	probe measuring the sound pressure at 2 different positions at a time
PU probe	probe measuring the sound pressure and the particle velocity at the same position
SNR	signal-to-noise ratio
SONAH	Statistically Optimized Near Field Acoustical Holography
SVD	singular value decomposition
Tbox	trim test rig for experimental characterization of vibro-acoustic properties of sound isolation materials